Imaging in three-dimensional waveguides with partial aperture data

Symeon Papadimitropoulos, Dimitrios A. Mitsoudis, Chrysoula Tsogka

Abstract

We consider the problem of imaging extended reflectors in three-dimensional acoustic waveguides using a planar array that is parallel to the waveguide's cross-section. Our data is the multiple-frequency array response matrix. To form an image we back-propagate a projection of the data on the propagating modes in the waveguide. The projection operator is adequately defined for any array aperture size and shape that covers fully or partially the waveguide cross-section. The properties of the imaging method are analyzed theoretically and its effectiveness is assessed by numerical experiments for scatterers and arrays of varying shape and size.

1 Introduction

We consider the problem of imaging extended reflectors in a three-dimensional, cylindrical, locally-perturbed acoustic waveguide. We examine two waveguide geometries: the *infinite* waveguide, in which the waveguide axis extends to infinity in both directions, and the *terminating* one where its axis is semi-infinite. These two geometries are illustrated in Figures 1 and 2. The remote sensing configuration consists of a single active planar array, denoted by $\mathcal{A}$, that is composed of N transducers which can be used as transmitters and receivers. The array is posed in the unperturbed part of the waveguide and may span the entire left cross-section of the waveguide, denoted by $\mathcal{C}$, or just a part of it. We refer to the former as the *full array-aperture* case and to the latter as the *partial*. Our data, for an angular frequency ω_l, are given in the form of an $N \times N$ complex symmetric matrix $[\Pi(\vec{\boldsymbol{x}}_s, \vec{\boldsymbol{x}}_r; \omega_l)]$, where the subscripts "$s, r$" denote source and receiver coordinates, respectively, and $l = 1, \ldots, N_f$, where N_f is the number of available frequencies. Specifically, the element $\Pi(\vec{\boldsymbol{x}}_s, \vec{\boldsymbol{x}}_r; \omega_l)$ is the response recorded at $\vec{\boldsymbol{x}}_r$ when a unit amplitude signal at frequency ω_l is sent from a point source at $\vec{\boldsymbol{x}}_s$.

Imaging in two-dimensional or three-dimensional infinite waveguides that are bounded in one direction has been traditionally related with applications in underwater acoustics, see, e.g., Refs. [8, 14, 16, 17, 22, 29]. Moreover, imaging in infinite or terminating waveguides that are bounded in two directions finds application in nondestructive testing[9, 12, 30] and in imaging in tunnels or pipes.[2, 20, 23, 25] Among the imaging methodologies that are widely used in waveguides with known and relatively simple geometry we refer to the linear sampling method (LSM),[3, 6, 7, 18] the factorization method,[1, 4] and reverse time migration methods or, their equivalent in the frequency domain, phase conjugation methods.[5, 15] In particular, Bourgeois and Lunéville[6] use a modal formulation of the LSM in order to detect sound-soft obstacles in an infinite cylindrical waveguide with sound-hard walls, and in a later work[7] they also apply modal formulations of the LSM and the factorization method, in the same waveguide setting, to reconstruct sound-soft or sound-hard cracks. Let us recall here that a boundary is described as being sound-soft (or sound-hard) whenever a Dirichlet (or Neumann) boundary condition is imposed. Monk and Selgas[18] employ the LSM and the Reciprocity Gap Method in order to detect penetrable, possibly anisotropic, scatterers in an infinite tubular waveguide that are allowed to touch the boundary of the waveguide. In a recent work,[3] Borcea, Cakoni and Meng introduce a linear sampling approach to detect local wall deformations and localized scatterers in a terminating tubular

waveguide with sound-hard walls. Arens, Gintides and Lechleiter[1] consider an infinite three-dimensional planar homogeneous waveguide to model the ocean environment, and they propose a factorization method for reconstructing penetrable scatterers. In another recent work, Borcea and Meng[4] present a comparative study of a factorization and a migration method for imaging sound-soft obstacles in a terminating acoustic waveguide with sound-hard walls.

One of the main characteristics in imaging a scatterer in a waveguide that is bounded in one or two directions is that, for a fixed frequency, there exists a specific number of modes that propagate at long distances and an infinite number of the so-called evanescent modes that rapidly decay with the propagating distance. Therefore, in practice, part of the information that is carried in the evanescent part of the wave field cannot be measured far from the scatterer, thus dictating that methods that are developed for imaging in waveguides should rely only on the propagating modes.[10, 19, 26]. Towards this direction, Dediu and McLaughlin[10] have proposed a method to recover weak inhomogeneities in an infinite strip that makes use of the eigenpairs of the far-field matrix in order to represent the solution of the linearized inverse scattering problem in terms of the propagating modes of the waveguide. Pinçon and Ramdani[19] study the problem of selective focusing on several small scatterers embedded in a two-dimensional infinite strip, by means of a time-reversal technique and the analysis of the spectral properties of the time-reversal operator. In our earlier work[26] we considered the problem of selective imaging of extended reflectors in a two-dimensional infinite strip with a full-aperture array and we have introduced a migration method that uses projections on low rank subspaces of a weighted modal projection of the array response matrix Π.

In this paper, following the methodology developed in our previous work,[28] we define an imaging functional that hinges upon the back-propagation of an appropriate projection of the array response matrix Π. The projection is fairly straightforward in the full-aperture case ($\mathcal{A} = \mathcal{C}$). Let us denote by $\{\Phi_n\}_{n=1}^{\infty}$ the usual orthonormal basis of $L^2(\mathcal{C})$ that consists of the orthonormal eigenfunctions of the negative transverse Laplacian in $\mathcal{C}$. We then project Π onto the M first eigenfunctions Φ_i, where M is the number of propagating modes. It turns out that the proposed imaging functional exhibits some interesting properties. For example, in a terminating waveguide we may show that the resulting image is directly related with the waveguide Green's function. Specifically, assuming that $\mathcal{A}$ is a continuous ideal array, we may prove that the image of a point source (or a point scatterer) is equal to (or to the square of) the imaginary part of the Green's function.

In this paper we consider the problem of imaging with partial aperture data. This is an interesting problem from a practical point of view since, in many realistic applications, we are rarely able to use arrays that entirely cover the waveguide cross-section. From the theoretical point of view, the main difficulty in the partial array-aperture case ($\mathcal{A} \subset \mathcal{C}$), lies in the fact that the Φ_n's are no longer orthogonal along the array. Our main contribution in this work is the construction of a finite-dimensional subspace of orthogonal functions with energy concentration properties, for two-dimensional planar arrays $\mathcal{A}$ of general shape.

Specifically, we introduce appropriate functions S_j, that are linear combinations of the eigenfunctions Φ_n with coefficients that depend on the eigenvalues and corresponding eigenvectors of the $M \times M$ real symmetric (Gram) matrix A_{arr}, whose (i, j) element is the integral over $\mathcal{A}$ of the product $\Phi_i(\cdot)\Phi_j(\cdot)$. The S_j are orthogonal along both $\mathcal{A}$ and $\mathcal{C}$, and we use them, instead of the Φ_n's, in order to project Π. Let us note that in the case of a two-dimensional waveguide, the array $\mathcal{A}$ is just a line segment posed perpendicular to the waveguide axis, and the matrix A_{arr} has a special structure. It is a Toeplitz-minus-Hankel matrix and this fact allows us to fully characterize its spectral properties and, also, identify the functions S_j as prolate or prolate-like wavefunctions.[27] The current three-dimensional setting is more interesting since the array instead of being just a segment can be a general planar array of arbitrary shape. In this case although we do not have an explicit characterization of the eigenpairs of the matrix A_{arr} and of the functions S_j, we can prove that all the eigenvalues of A_{arr} lie in $[0, 1]$, and that the functions S_j exhibit energy concentration properties similar to those of the prolates.

Projecting the data Π using the S_j functions has important implications in imaging. We can show for example, that as long as the minimum eigenvalue of the matrix A_{arr} remains above a threshold, then we do not lose any information and we may recover the same image as if we were using a full aperture array. This result holds under the assumptions of the linearized Born approximation. Moreover, a careful numerical investigation indicates that the number of the eigenvalues of A_{arr} that are close to one is approximately equal to $M\,|\mathcal{A}|/|\mathcal{C}|$, where $|\cdot|$ denotes area, irrespectively of the shape of the array, thus extending to this case analogous results for the two-dimensional waveguide.[26, 27]

The performance of the proposed imaging method is assessed with numerical experiments where the array response matrix is created by means of the linearized Born approximation. We consider a uniform waveguide with rectangular cross-section that allows us to have an analytical expression for the Green's function, thus avoiding to solve numerically the full wave equation in three dimensions. We treat the full- and partial-aperture cases and experiment with various array sizes and shapes. We also investigate the robustness of the method to measurement noise. The use of multiple frequencies is also examined and reveals a significant improvement in the effectiveness of our method, allowing us to create good images with quite small arrays.

The paper is organized as follows. In Section 2 we present the problem setup. Section 3 is devoted to the description of our imaging approach in the case of a full-aperture array. In Section 4 we examine the partial-aperture case, and explore the properties of the matrix A_{arr} and the behavior of the functions S_j. Finally, in Section 5 we assess the performance of our approach with numerical simulations for various scatterer and array geometries.

2 Problem setup

In this work, we study the problem of imaging an extended reflector embedded in a three-dimensional cylindrical, locally perturbed waveguide using an active planar array that is parallel to the waveguide cross-section. We consider a three-dimensional Cartesian coordinate system $\vec{\boldsymbol{x}} = (z, \boldsymbol{z}') \in \mathbb{R}^3$, and we assume that the axis of the unperturbed waveguide is parallel to the z–axis, hereinafter referred to as the range. The cross-range coordinates $\boldsymbol{z}' = (x, y)$ lie on the transverse xy–plane, and x is taken to be positive downwards. In what follows, we distinguish two cases for the physical domain: (i) The *infinite waveguide*, where waves travel infinitely as the range coordinate $z \to \pm\infty$, and (ii) the *terminating waveguide*, i.e. a semi-infinite waveguide where waves propagate infinitely only as $z \to -\infty$.

Specifically, let Ω^{i} be a three-dimensional infinite waveguide, as shown in Figure 1, that consists of three parts: two semi-infinite cylindrical waveguides Ω_{L^-} and Ω_{L^+} of constant cross-section $\mathcal{C}$ for ranges $z < L^-$ and $z > L^+$, and a bounded domain Ω^{i}_L for $L^- < z < L^+$ where the cross-section may vary with range. Thus $\Omega^{\text{i}} := \Omega_{L^-} \cup \Omega^{\text{i}}_L \cup \Omega_{L^+}$. Moreover, we assume that the cross-section $\mathcal{C}$ is a bounded, Lipschitz domain on the transverse xy–plane, and that $\Omega_{L^\pm}$ are filled with a homogeneous medium, while the medium in the intermediate region Ω^{i}_L may be inhomogeneous.

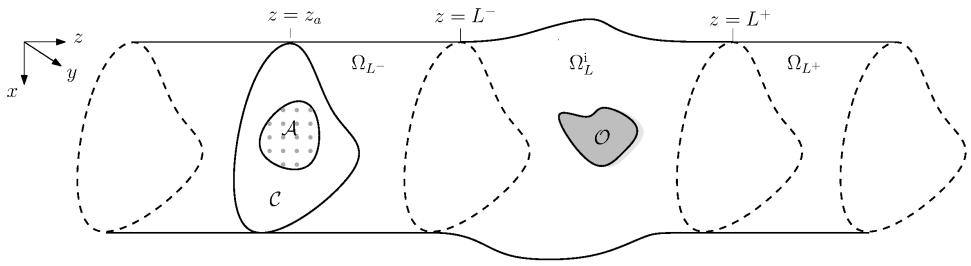

Figure 1: Schematic representation of an infinite three-dimensional waveguide $\Omega^{\text{i}} := \Omega_{L^-} \cup \Omega^{\text{i}}_L \cup \Omega_{L^+}$.

Analogously, the terminating waveguide Ω^{t} (see Figure 2) is a semi-infinite three-dimensional waveguide consisting of two parts: a semi-infinite cylindrical waveguide Ω_{L^-} (defined as before for range $z < L$), and a bounded domain Ω_L^{t} where the cross-section may vary with range and/or the medium may be inhomogeneous. In this case we have $\Omega^{\mathrm{t}} := \Omega_{L^-} \cup \Omega_L^{\mathrm{t}}$.

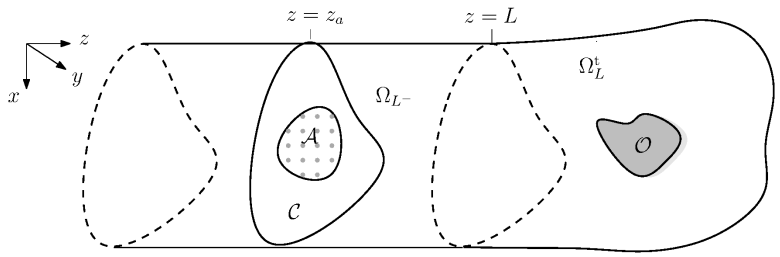

Figure 2: Schematic representation of a terminating three-dimensional waveguide $\Omega^{\mathrm{t}} := \Omega_{L^-} \cup \Omega_L^{\mathrm{t}}$.

In order to simplify things, we restrict ourselves to the acoustic case and assume that the waveguide has a sound-soft boundary. However, our approach generalizes to other boundary conditions as well. An active planar array $\mathcal{A}$ that contains N transducers is placed parallel to the waveguide's cross-section at range $z = z_a$ in Ω_{L^-}. The array is composed of N transducers that act as sources and receivers and are assumed to be uniformly distributed. Specifically, let $\mathcal{A}$ be a two-dimensional point lattice where each lattice cell is a square of sidelength h and the transducers are located at the lattice points. We will examine two cases: a) A full-aperture array, that is an array that spans the entire cross-section $\mathcal{C}$, i.e. $\mathcal{A} \equiv (h\mathbb{Z}^2 \cap \mathcal{C})$, and b) a partial-aperture array where the array spans only part of $\mathcal{C}$, i.e. $\mathcal{A} \subset (h\mathbb{Z}^2 \cap \mathcal{C})$. Moreover, h is considered to be relatively small, typically a fraction of the wavelength λ. In these two configurations our goal is to create images that will allow us to locate an extended reflector $\mathcal{O}$ that is contained somewhere in Ω_L^{i} (or Ω_L^{t}) in the case of the infinite (or terminating) waveguide. The term extended indicates that the reflector is comparable in size to λ.

Each element in the array acts as a point-source that emits a continuous time-harmonic signal of angular frequency ω. Therefore, the total field due to a point-source located, say, at $\vec{\boldsymbol{x}}_s$ satisfies the Helmholtz equation

$$-\Delta p^{\mathrm{tot}}(\vec{\boldsymbol{x}};\omega) - k^2\eta(\vec{\boldsymbol{x}})\, p^{\mathrm{tot}}(\vec{\boldsymbol{x}};\omega) = \delta(\vec{\boldsymbol{x}} - \vec{\boldsymbol{x}}_s), \quad \vec{\boldsymbol{x}} \in \Omega \setminus \overline{\mathcal{O}}, \tag{1}$$

where $k = \omega/c_0$ is the (real) wavenumber, $\eta(\vec{\boldsymbol{x}}) = c_0^2/c^2(\vec{\boldsymbol{x}})$ is the index of refraction, and $\Omega = \Omega^{\mathrm{i}}$ (or Ω^{t}) in the case of the infinite (or terminating) waveguide. Equation (1) is supplemented with homogeneous Dirichlet boundary conditions on $\partial\Omega$, a Dirichlet or a Neumann boundary condition on $\partial\mathcal{O}$ depending whether the scatterer is assumed to be sound-soft or sound-hard, respectively, and an appropriate radiation condition ensuring that the field is outgoing as the range tends to $\pm\infty$ (or $-\infty$) in the case where $\Omega = \Omega^{\mathrm{i}}$ (or Ω^{t}).

Moreover, the incident field at a point $\vec{\boldsymbol{x}} \in \Omega$, due to a point-source situated at $\vec{\boldsymbol{x}}_s$ and for a single frequency ω, is given by the Green's function, denoted by $G(\vec{\boldsymbol{x}}, \vec{\boldsymbol{x}}_s;\omega)$. Hence $G(\vec{\boldsymbol{x}}, \vec{\boldsymbol{x}}_s;\omega)$ solves

$$-\Delta G(\vec{\boldsymbol{x}}, \vec{\boldsymbol{x}}_s;\omega) - k^2\eta(\vec{\boldsymbol{x}})G(\vec{\boldsymbol{x}}, \vec{\boldsymbol{x}}_s;\omega) = \delta(\vec{\boldsymbol{x}} - \vec{\boldsymbol{x}}_s), \quad \vec{\boldsymbol{x}} \in \Omega, \tag{2}$$

along with Dirichlet boundary conditions on $\partial\Omega$, and the appropriate radiation condition.

In the homogeneous cylindrical parts $\Omega_{L^\pm}$ of the waveguide, with constant cross-section $\mathcal{C}$, we consider the Dirichlet eigenvalue problem for the negative transverse Laplacian, i.e.

$$\begin{aligned} -\Delta_{\boldsymbol{z}'}\Phi &= \mu\,\Phi \quad \text{in } \mathcal{C}, \\ \Phi &= 0 \quad \text{on } \partial\mathcal{C}. \end{aligned} \tag{3}$$

It is well-known that the spectrum of $-\Delta_{\boldsymbol{z}'}$ is discrete. The eigenvalues μ_n are positive $0 < \mu_1 \le \mu_2 \le \ldots \to \infty$, and the corresponding orthonormal eigenfunctions Φ_n form a complete, orthonormal basis in $L^2(\mathcal{C})$. From now

on, let M be the number of propagating modes in $\Omega_{L^\pm}$, i.e. an index such that the constant wavenumber k^2 satisfies

$$\mu_M < k^2 < \mu_{M+1},$$

and let

$$\beta_n := \begin{cases} \sqrt{k^2 - \mu_n}, & 1 \le n \le M, \\ \mathrm{i}\sqrt{\mu_n - k^2}, & n \ge M+1. \end{cases} \tag{4}$$

We assume that the data that we have in our disposal for imaging consist of the array measurements given in the form of a matrix, denoted Π, which will be referred to as the array response matrix. Specifically, Π is an $N \times N$ complex symmetric (not Hermitian) matrix whose (r,s)-entry contains the wave field recorded at the r-th receiver, located at $\vec{\boldsymbol{x}}_r$, when the s-th source, placed at $\vec{\boldsymbol{x}}_s$, emits a time-harmonic signal. In particular, we shall use the array response matrix for the scattered field that is due to the presence of an extended reflector $\mathcal{O}$ located somewhere in Ω_L^{i} or in Ω_L^{t}. As usual, the scattered field is determined by subtracting the incident field from the total field.

In order to successfully image a reflector we have to define an appropriate imaging functional and a search domain $\mathcal{S} \subset \Omega_L^{\mathrm{i}}$ (or $\mathcal{S} \subset \Omega_L^{\mathrm{t}}$). We discretize $\mathcal{S}$ with a (usually rectangular) three-dimensional grid and we evaluate the imaging functional at the grid points, see for example Figure 3 for the terminating waveguide case. Then we graphically display these values to form an image that is expected to exhibit peaks at the location of the scatterer.

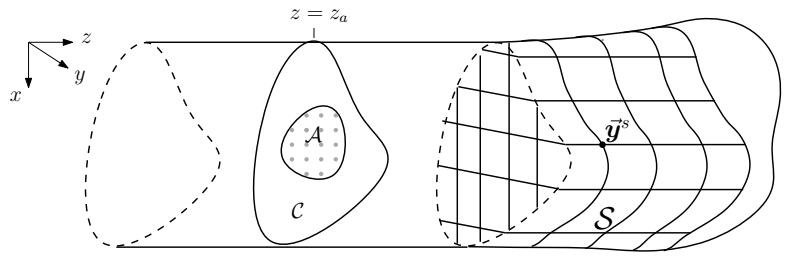

Figure 3: Schematic representation of the discretization of a search domain in a terminating three-dimensional waveguide Ω^{t}.

3 Imaging with a full-aperture array

In this section we consider the case of a terminating waveguide as shown in Figure 2. To motivate our imaging process we start with the problem of detecting the location of a point source of unit strength that transmits a signal which is received by the elements of a passive planar array $\mathcal{A}$ that covers the entire waveguide cross-section $\mathcal{C}$. This problem is commonly referred to as the *passive imaging problem*. In the second part of this section we examine the *active imaging problem* where the objective is to detect the position of a single scatterer with unit reflectivity. In this case $\mathcal{A}$ is an active source-receiver array. In both cases the array $\mathcal{A}$ is placed at range $z = z_a$ ($z_a < L$), consists of N transducers and, as already mentioned in Section 2, is defined as $\mathcal{A} \equiv (h\mathbb{Z}^2 \cap \mathcal{C})$. In order to provide some insight into the properties of the imaging functional that we are going to introduce next, we will first consider the idealized case of a continuous array that entirely covers $\mathcal{C}$.

3.1 The passive imaging problem

In our earlier work[28] we have proposed an imaging approach for the passive imaging problem in the case of a two-dimensional terminating waveguide. The extension to the current three-dimensional setting is fairly straightforward hence here we will briefly summarize its main ingredients.

The proposed imaging functional is motivated by phase conjugation and its well-known time-domain equivalent which is time reversal. The basic idea is the following: For the passive problem of imaging a single point source located at $\vec{\boldsymbol{x}}_s = (z_s, \boldsymbol{z}'_s)$, the response matrix turns out to be an $N \times 1$ vector whose r-th component is simply the Green's function evaluated at an arbitrary point $\vec{\boldsymbol{x}}_r = (z_a, \boldsymbol{z}'_r)$ that lies on the surface of the ideal array $\mathcal{A}$, i.e.

$$\Pi(\vec{\boldsymbol{x}}_r; \omega) = G(\vec{\boldsymbol{x}}_r, \vec{\boldsymbol{x}}_s; \omega). \tag{5}$$

To simplify our notation, as long as we consider a monochromatic source we drop parameter ω from the Green's function, the array response matrix, etc. Hereinafter, the dependence in ω will be explicitly displayed whenever we refer to multifrequency data.

Next, assuming that the array is capable of recording the field and its normal derivative, we conjugate the field and retransmit it to a search point $\vec{\boldsymbol{y}}^{\mathrm{s}} \in S$ according to Huygen's principle that is expressed mathematically via the Helmholtz-Kirchhoff integral.[15, 17] Thus we may define the imaging functional

$$\mathcal{I}(\vec{\boldsymbol{y}}^{\mathrm{s}}) := \int_{\mathcal{A}} \Big(\overline{G(\vec{\boldsymbol{x}}_r, \vec{\boldsymbol{x}}_s)} \nabla G(\vec{\boldsymbol{x}}_r, \vec{\boldsymbol{y}}^{\mathrm{s}}) - G(\vec{\boldsymbol{x}}_r, \vec{\boldsymbol{y}}^{\mathrm{s}}) \overline{\nabla G(\vec{\boldsymbol{x}}_r, \vec{\boldsymbol{x}}_s)} \Big) \cdot \hat{\boldsymbol{n}} \, d\boldsymbol{z}', \tag{6}$$

where $\hat{\boldsymbol{n}}$ is the outward unit normal vector to $\mathcal{A}$. As we shall see in a while this functional possesses interesting theoretical properties.

This procedure is well established in the case of a closed, ideal array that surrounds the source,[15, 17] and Porter[21] has proven that in this case and for a lossless medium (i.e. when $k^2\eta(\vec{\boldsymbol{x}})$ is real) it holds that $\mathcal{I}(\vec{\boldsymbol{y}}^{\mathrm{s}}) = 2i \operatorname{Im}\{\widehat{G}(\vec{\boldsymbol{y}}^{\mathrm{s}}, \vec{\boldsymbol{x}}_s)\}$.

Of course, it is well-known that it is very difficult to create an array that is able to record both the field and its normal derivative. However, in our case of a terminating waveguide and for an array that does not surround the source but rather it fully covers the waveguide cross-section, we may define an imaging functional that only requires the knowledge of the field and not of its derivatives. The definition relies on the following Kirchhoff-Helmholtz type identity:

Proposition 1 (Kirchhoff-Helmholtz identity) *Let Ω^{t} be the terminating waveguide that we have described in Section 2 and is shown in Figure 2. For any $z_a < L$, by slightly abusing the notation, let $\mathcal{A} = \{z_a\} \times \mathcal{C}$ be an artificial boundary posed at range $z = z_a$ and Ω_{z_a} be the bounded part of the waveguide Ω^{t} that is defined for range $z > z_a$. Let $\vec{\boldsymbol{x}}_1, \vec{\boldsymbol{x}}_2 \in \Omega_{z_a}$. Then*

$$G(\vec{\boldsymbol{x}}_1, \vec{\boldsymbol{x}}_2) - \overline{G(\vec{\boldsymbol{x}}_1, \vec{\boldsymbol{x}}_2)} = \int_{\mathcal{A}} \Big(\overline{G(\vec{\boldsymbol{y}}, \vec{\boldsymbol{x}}_1)} \nabla G(\vec{\boldsymbol{y}}, \vec{\boldsymbol{x}}_2) - G(\vec{\boldsymbol{y}}, \vec{\boldsymbol{x}}_2) \overline{\nabla G(\vec{\boldsymbol{y}}, \vec{\boldsymbol{x}}_1)} \Big) \cdot \hat{\boldsymbol{n}} \, d\boldsymbol{z}', \tag{7}$$

where $\hat{\boldsymbol{n}}$ is the outward unit normal vector to $\mathcal{A}$. Moreover,

$$G(\vec{\boldsymbol{x}}_1, \vec{\boldsymbol{x}}_2) - \overline{G(\vec{\boldsymbol{x}}_1, \vec{\boldsymbol{x}}_2)} = 2i \sum_{i=1}^{M} \beta_i \, \overline{G_i(z_a, \vec{\boldsymbol{x}}_1)} \, G_i(z_a, \vec{\boldsymbol{x}}_2), \tag{8}$$

where $G_i(z_a, \cdot)$ is the i-th Fourier coefficient of the Green's function with respect to the orthonormal basis $\{\Phi_n\}_{n=1}^{\infty}$ of $L^2(\mathcal{C})$, i.e.,

$$G_i(z_a, \cdot) = \int_{\mathcal{C}} G\big((z_a, \boldsymbol{z}'), \cdot\big) \, \Phi_i(\boldsymbol{z}') \, d\boldsymbol{z}', \quad i = 1, \ldots, M. \tag{9}$$

In Ref. [28], Appendix A, we have proven the analogue of Proposition 1 in the case of a two-dimensional terminating waveguide. The proof uses the reciprocity relation of the Green's function and properly exploits properties of the Dirichlet-to-Neumann map on the artificial boundary $\mathcal{A}$. The generalization to the present three-dimensional setting is straightforward hence we omit it.

Thus, in view of Proposition 1 and (5), we define our passive imaging functional, for a generic response matrix $\Pi(\vec{\boldsymbol{x}}_r) = \Pi(z_a, \boldsymbol{z}'_r)$, as

$$\mathcal{I}^{\mathrm{p}}(\vec{\boldsymbol{y}}^{\mathrm{s}}) = \sum_{i=1}^{M} \beta_i \overline{\mathbb{Q}_i}\; G_i(z_a, \vec{\boldsymbol{y}}^{\mathrm{s}}), \tag{10}$$

where the superscript 'p' denotes the passive imaging case,

$$\mathbb{Q}_i = \int_{\mathcal{A}} \Pi(z_a, \boldsymbol{z}'_r)\Phi_i(\boldsymbol{z}'_r)\; d\boldsymbol{z}'_r, \quad i = 1, \ldots, M, \tag{11}$$

is the projection of Π on the M-first eigenfunctions Φ_i, with M being the number of propagating modes in Ω_{L^-}, and β_i are the horizontal wavenumbers given by (4).

Note that in the the special case where $\Pi(\vec{\boldsymbol{x}}_r)$ has the form shown in (5), i.e. it incorporates the field due to a point source of unit strength located at $\vec{\boldsymbol{x}}_s$, then we may prove the following lemma, that verifies the previously mentioned result by Porter[21] in our case.

Lemma 1 (Point source imaging) *For a point source of unit strength located at $\vec{\boldsymbol{x}}_s$ corresponding to array data $\Pi(\vec{\boldsymbol{x}}_r)$ as in* (5)*, the passive imaging functional $\mathcal{I}^{\mathrm{p}}(\vec{\boldsymbol{y}}^{\mathrm{s}})$ defined by* (10)-(11) *is equal to the imaginary part of the Green's function from $\vec{\boldsymbol{x}}_s$ to $\vec{\boldsymbol{y}}^{\mathrm{s}}$, i.e., we have*

$$\mathcal{I}^{\mathrm{p}}(\vec{\boldsymbol{y}}^{\mathrm{s}}) = \operatorname{Im} G(\vec{\boldsymbol{y}}^{\mathrm{s}}, \vec{\boldsymbol{x}}_s). \tag{12}$$

Lemma 1 is an interesting result which tells us that in this case the quality of the focusing of the proposed imaging functional is controlled by the imaginary part of the Green's function in the waveguide. The proof is an immediate consequence of the Kirchhoff-Helmholtz identity that is stated in Proposition 1.

To sum up, the imaging process for the passive imaging case can be written in the form of the following algorithm.

Algorithm 1 ***(Passive Imaging – Full-aperture array)***
Given the array data $\Pi(\vec{\boldsymbol{x}}_r)$, $r = 1, \ldots, N$:

(a) We project the recorded field $\Pi(\vec{\boldsymbol{x}}_r)$ onto the M-first eigenfunctions Φ_i, $i = 1, \ldots, M$, of the negative transverse Laplacian in $\mathcal{C}$, see (3)*, i.e.*

$$\mathbb{Q}_i = \int_{\mathcal{A}} \Pi(z_a, \boldsymbol{z}'_r)\Phi_i(\boldsymbol{z}'_r)\; d\boldsymbol{z}'_r, \quad i = 1, \ldots, M, \tag{13}$$

where M is the number of propagating modes in Ω_{L^-}.

(b) For each $\vec{\boldsymbol{y}}^{\mathrm{s}} \in \mathcal{S}$ we evaluate the imaging functional

$$\mathcal{I}^{\mathrm{p}}(\vec{\boldsymbol{y}}^{\mathrm{s}}) = \sum_{i=1}^{M} \beta_i\, \overline{\mathbb{Q}_i}\; G_i(z_a, \vec{\boldsymbol{y}}^{\mathrm{s}}), \tag{14}$$

where G_i are defined in (9)*.*

Remark 1 *In the definition of the projected vector $\mathbb{Q}$, see* (13)*, we treat $\mathcal{A}$ as an ideal continuous array. However, in practice, $\mathcal{A}$ consists of N discrete elements therefore the definition is modified as*

$$\mathbb{Q}_i := h^2 \sum_{r=1}^{N} \Pi(z_a, \boldsymbol{z}'_r)\, \Phi_i(\boldsymbol{z}'_r), \quad i = 1, \ldots, M,$$

where h is the lattice parameter.

3.2 The active imaging problem

Next, we deal with the active imaging problem. Our objective is to detect the position $\vec{\boldsymbol{x}}_* = (z_*, \boldsymbol{z}'_*)$ of a single point scatterer with unit reflectivity. Now $\mathcal{A}$ is an active source-receiver array and the (r, s) entry of the associated array response matrix is specified by the scattered field recorded at $\vec{\boldsymbol{x}}_r$ when the point reflector at $\vec{\boldsymbol{x}}_*$ is illuminated by a signal of unit strength emitted from a point source at $\vec{\boldsymbol{x}}_s$. Therefore, $\Pi(\vec{\boldsymbol{x}}_r, \vec{\boldsymbol{x}}_s) = k^2\, G(\vec{\boldsymbol{x}}_*, \vec{\boldsymbol{x}}_s) G(\vec{\boldsymbol{x}}_r, \vec{\boldsymbol{x}}_*)$, and suppressing the multiplicative constant k^2 we may assume that

$$\Pi(\vec{\boldsymbol{x}}_r, \vec{\boldsymbol{x}}_s) = G(\vec{\boldsymbol{x}}_*, \vec{\boldsymbol{x}}_s) G(\vec{\boldsymbol{x}}_r, \vec{\boldsymbol{x}}_*). \tag{15}$$

The imaging procedure in this case, under the assumption of a continuous array is described in Algorithm 2.

Algorithm 2 ***(Active Imaging – Full-aperture array)***
Given the array data $\Pi(\vec{\boldsymbol{x}}_r, \vec{\boldsymbol{x}}_s)$, $r, s = 1, \ldots, N$*:*

(a) We define the projected response matrix $\mathbb{Q}$ *by*

$$\mathbb{Q}_{ij} = \int_{\mathcal{A}} \int_{\mathcal{A}} \Pi(\vec{\boldsymbol{x}}_r, \vec{\boldsymbol{x}}_s) \Phi_i(\boldsymbol{z}'_s) \Phi_j(\boldsymbol{z}'_r)\; d\boldsymbol{z}'_s d\boldsymbol{z}'_r, \quad i, j = 1, \ldots, M. \tag{16}$$

(b) For each $\vec{\boldsymbol{y}}^{\,\mathrm{s}} \in \mathcal{S}$ *we evaluate the imaging functional*

$$\mathcal{I}^{\mathrm{a}}(\vec{\boldsymbol{y}}^{\,\mathrm{s}}) = \sum_{i=1}^{M} \sum_{j=1}^{M} \beta_i\; \beta_j\; \overline{\mathbb{Q}_{ij}}\; G_i(z_a, \vec{\boldsymbol{y}}^{\,\mathrm{s}})\; G_j(z_a, \vec{\boldsymbol{y}}^{\,\mathrm{s}}), \tag{17}$$

where the superscript 'a' denotes the active imaging case and $G_i(z_a, \cdot)$ *are as in* (9)*.*

Note that the definitions (16) and (17) concern a generic reflector. In the special case where the reflector is a point scatterer located at $\vec{\boldsymbol{x}}_*$, and the array response matrix is given by (15), it is easy to show the following lemma (the proof follows from the Kirchhoff-Helmholtz identity).

Lemma 2 (Point reflector imaging) *For a point scatterer with unit reflectivity located at* $\vec{\boldsymbol{x}}_*$*, corresponding to array data* $\Pi(\vec{\boldsymbol{x}}_r, \vec{\boldsymbol{x}}_s)$ *as in* (15)*, the active imaging functional* $\mathcal{I}^{\mathrm{a}}(\vec{\boldsymbol{y}}^{\,\mathrm{s}})$ *defined in Algorithm 2 is equal to the square of the imaginary part of the Green's function from* $\vec{\boldsymbol{x}}_*$ *to* $\vec{\boldsymbol{y}}^{\mathrm{s}}$*, i.e., we have*

$$\mathcal{I}^{\mathrm{a}}(\vec{\boldsymbol{y}}^{\,\mathrm{s}}) = \Big(\mathrm{Im}\big(\mathrm{G}(\vec{\boldsymbol{y}}^{\,\mathrm{s}}, \vec{\boldsymbol{x}}_*)\big)\Big)^2. \tag{18}$$

Lemma 2 characterizes the point spread function of the imaging functional $\mathcal{I}^{\mathrm{a}}(\vec{\boldsymbol{y}}^{\,\mathrm{s}})$. As in the passive case the quality of the focusing of the proposed imaging functional is controlled by the imaginary part of the Green's function in the waveguide.

4 Imaging with a partial-aperture array

In this section we concentrate on the main subject of this paper which is the study of the imaging problem that is stated in Section 2 with an array that spans only part of the waveguide's cross-section $\mathcal{C}$. The approach that we have briefly discussed in the preceding section for the full-aperture case, needs to be modified in order to create images of good quality with smaller arrays that do not entirely cover the waveguide cross-section. The main reason for this, is that in the partial aperture case the eigenfunctions Φ_i, $i = 1, \ldots, M$, of the negative transverse Dirichlet-Laplacian that we have employed in (13) and (16) in order to define the projected matrix $\mathbb{Q}$ are no longer orthonormal along the array $\mathcal{A}$.

In what follows we will construct a finite-dimensional subspace of appropriately chosen functions $S_j(\boldsymbol{z}')$, $\boldsymbol{z}' \in \mathcal{C}$, that possess the interesting property of being doubly orthogonal, i.e. orthogonal along the array $\mathcal{A}$

and along the cross-section $\mathcal{C}$, and exhibit very good concentration properties. Then we are going to use these functions in order to project the array response matrix Π.

As we shall immediately see, the real symmetric matrix $A_{\rm arr}$ with entries

$$(A_{\rm arr})_{ij} = \int_{\mathcal{A}} \Phi_i(\boldsymbol{z}')\, \Phi_j(\boldsymbol{z}')\, d\boldsymbol{z}', \quad i,j = 1,\ldots,M, \tag{19}$$

plays a key role in this construction.

4.1 Properties of the matrix $A_{\rm arr}$

Let $\{\nu_n\}$ denote the eigenvalues of the matrix $A_{\rm arr}$ that is defined in (19) (written in decreasing order) and $\{\boldsymbol{w}^{(n)}\}$ be the corresponding orthonormal eigenvectors. From now on let W denote the $M \times M$ orthogonal matrix $W = [\boldsymbol{w}^{(1)}, \ldots, \boldsymbol{w}^{(M)}]$. It is well-known that the eigenvalues ν_n are real. Moreover, the following lemma holds:

Lemma 3 *The matrix $A_{\rm arr}$ is positive semi-definite and for all $n = 1,\ldots,M$, it holds that $0 \le \nu_n \le 1$.*

Proof. Let $\boldsymbol{v} = (v_1,\ldots,v_M)^T \in \mathbb{R}^M$, $\boldsymbol{v} \neq \boldsymbol{0}$, and

$$\alpha_{\boldsymbol{v}}(\boldsymbol{z}') = \sum_{k=1}^{M} v_k\, \Phi_k(\boldsymbol{z}'), \quad \boldsymbol{z}' \in \mathcal{C}.$$

Then

$$\begin{aligned} \boldsymbol{v}^T A_{\rm arr} \boldsymbol{v} &= \sum_{i=1}^{M}\sum_{j=1}^{M} v_i v_j (A_{\rm arr})_{ij} = \sum_{i=1}^{M}\sum_{j=1}^{M} v_i v_j \int_{\mathcal{A}} \Phi_i(\boldsymbol{z}')\, \Phi_j(\boldsymbol{z}')\, d\boldsymbol{z}' \\ &= \int_{\mathcal{A}} \sum_{i=1}^{M} v_i \Phi_i(\boldsymbol{z}') \sum_{j=1}^{M} v_j \Phi_j(\boldsymbol{z}')\, d\boldsymbol{z}' = \int_{\mathcal{A}} \alpha_{\boldsymbol{v}}^2(\boldsymbol{z}')\, d\boldsymbol{z}' \ge 0. \end{aligned}$$

Moreover,

$$\int_{\mathcal{A}} \alpha_{\boldsymbol{v}}^2(\boldsymbol{z}')\, d\boldsymbol{z}' \le \int_{\mathcal{C}} \alpha_{\boldsymbol{v}}^2(\boldsymbol{z}')\, d\boldsymbol{z}' = \sum_{i=1}^{M} v_i^2 =: \|\boldsymbol{v}\|_2^2,$$

hence

$$0 \le \boldsymbol{v}^T A_{\rm arr} \boldsymbol{v} \le \|\boldsymbol{v}\|_2^2, \quad \text{for all } \boldsymbol{v} \neq \boldsymbol{0}. \tag{20}$$

Finally, from the well-known Rayleigh quotient theorem,[13, p. 235] it also holds that the maximum eigenvalue ν_1 satisfies:

$$\nu_1 = \max_{\boldsymbol{v}\neq\boldsymbol{0}} \frac{\boldsymbol{v}^T A_{\rm arr} \boldsymbol{v}}{\|\boldsymbol{v}\|_2^2} \overset{(20)}{\le} 1.$$

□

Remark 2 *For a two-dimensional waveguide of width D, the vertical array is simply an interval of width $l_{\rm arr} \le D$, and the matrix $A_{\rm arr}$ has a very special structure, it is a Toeplitz-minus-Hankel matrix. Then it may be shown that its eigenvalues cluster near 0 and 1, and the number of 'significant' (in the sense that they are not close to zero) eigenvalues is approximately equal to*

$$\Big[M\,\frac{l_{\rm arr}}{D}\Big] \approx \Big[\frac{l_{\rm arr}}{\lambda/2}\Big],$$

where λ is the probe wavelength. Furthermore, the eigenvectors may be identified as discrete prolate or prolate-like wavefunctions.[27]

In view of the above remark we have numerically investigated whether these properties still hold in the current setting where the array is a two-dimensional region. Our results indicate that the eigenvalues of $A_{\rm arr}$ still cluster near 0 and 1, and the value $M \cdot |\mathcal{A}|/|\mathcal{C}|$, where $|\mathcal{A}|$ and $|\mathcal{C}|$ denote the areas of $\mathcal{A}$ and $\mathcal{C}$, respectively, provides a good estimate for the number of the "most significant" among them.

To illustrate our observations we consider the following example: Let the cross-section $\mathcal{C}$ of the unperturbed part of the waveguide be the rectangle $\mathcal{C} = [0, D] \times [0, W]$, where $D = 10\lambda_0$, $W = 20\lambda_0$, and λ_0 is a reference wavelength that corresponds to a reference wavenumber $k_0 = \pi/10$. Then $|\mathcal{C}| = D \cdot W$ is the area of the rectangular cross-section. We consider arrays of four different shapes: A rectangle, an ellipse, a quadrifolium, and an annular ellipse, as shown in the left column of Figure 4 from top to bottom, respectively. Specifically, the arrays that are shown there cover approximately 40% of the area $|\mathcal{C}|$. In the second to fourth columns of Figure 4 we plot the eigenvalue distribution of the $M \times M$ matrix $A_{\rm arr}$ for these four array types, for arrays of different area. Recall that M is the number of propagating modes and in this example we consider a single frequency that corresponds to a wavenumber $k = 0.9875k_0$, which leads to the value $M = 584$. Specifically, the second column corresponds to arrays with area approximately equal to 40% of $|\mathcal{C}|$, in the third column $|\mathcal{A}| \approx 0.25|\mathcal{C}|$, while in the fourth one $|\mathcal{A}| \approx 0.04|\mathcal{C}|$. Note that in the fourth column we plot just the first 50 (larger) eigenvalues since the rest decrease rapidly to zero. In all these plots a vertical line (typed in red) indicates the value $\frac{M|\mathcal{A}|}{|\mathcal{C}|}$. As one may immediately verify, in all four array types it seems that, irrespective of the shape of the array, the value $M \cdot |\mathcal{A}|/|\mathcal{C}|$ is an accurate estimate for the number of "significant" eigenvalues of $A_{\rm arr}$.

Now we are in a position to introduce the functions S_j that we are going to use in order to project the array response matrix Π.

4.2 Definition and properties of the functions S_j

Definition 1 *For any $\varepsilon \in (0, 1)$, let M_ε be the largest index in $\{1, 2, \ldots, M\}$ such that $\nu_{M_\varepsilon} \geq \varepsilon$.*

Then for $\boldsymbol{z}' \in \mathcal{C}$ we define the functions

$$S_j(\boldsymbol{z}') = \frac{1}{\nu_j} \sum_{i=1}^{M} w_i^{(j)} \Phi_i(\boldsymbol{z}'), \quad j = 1, 2, \ldots, M_\varepsilon, \tag{21}$$

where $w_i^{(j)}$, $i = 1, \ldots, M$, are the components of the eigenvector $\boldsymbol{w}^{(j)}$ that corresponds to the eigenvalue ν_j of the matrix $A_{\rm arr}$.

We also define W_ε as the $M \times M_\varepsilon$ matrix with columns the eigenvectors of the matrix $A_{\rm arr}$:

$$W_\varepsilon = [\boldsymbol{w}^{(1)}, \ldots, \boldsymbol{w}^{(M_\varepsilon)}]. \tag{22}$$

The functions S_j possess interesting properties that are summarized in the following proposition.

Proposition 2 *The functions S_j, $j = 1, \ldots, M_\varepsilon$, are doubly orthogonal in the sense that*

$$(S_k, S_l)_{L^2(\mathcal{C})} = \frac{1}{\nu_k \nu_l} \delta_{kl} \quad \text{and} \quad (S_k, S_l)_{L^2(\mathcal{A})} = \frac{1}{\nu_k} \delta_{kl},$$

where $(\cdot, \cdot)$ denotes the usual L^2–inner product and δ_{kl} is the Kronecker delta. Moreover, they exhibit maximum fractional concentration of energy in $\mathcal{A}$. Specifically, it holds that

$$\frac{\|S_k\|_{L^2(\mathcal{A})}}{\|S_k\|_{L^2(\mathcal{C})}} = \nu_k^{1/2}, \quad k = 1, \ldots, M_\varepsilon.$$

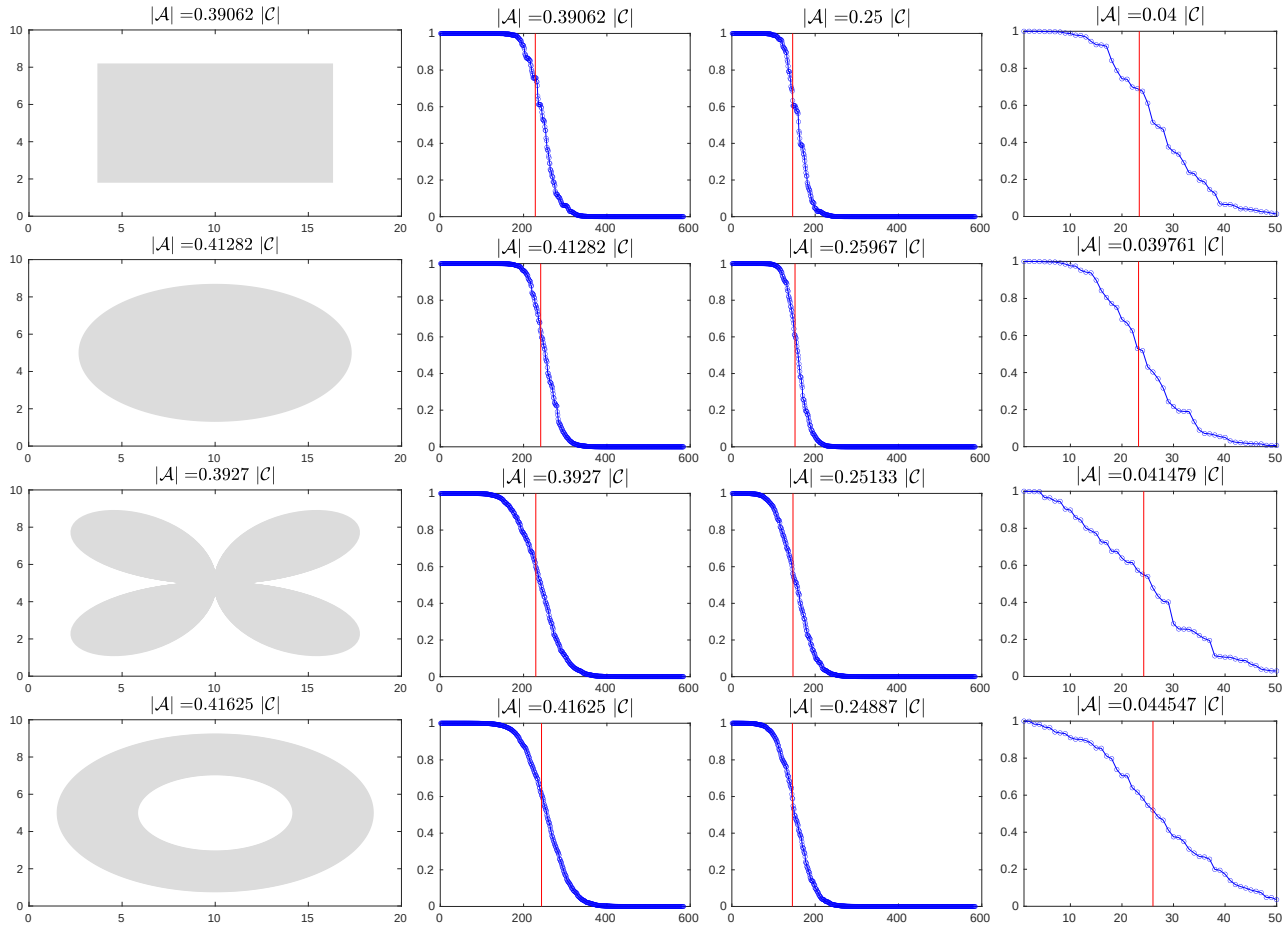

Figure 4: Array shape (left column) and singular values of A_{arr} (columns 2–4). Array shape from top to bottom: Rectangle, ellipse, quadrifolium and annular ellipse. The eigenvalues shown in columns 2–4 correspond to arrays that cover approximately 40%, 25% and 4% of $|\mathcal{C}|$, respectively. The vertical line (typed in red) in columns 2–4 indicates the value $\frac{M|\mathcal{A}|}{|\mathcal{C}|}$.

Proof. The first orthogonality relation results from the orthonormality of the eigenfunctions $\{\Phi_i\}$ and of the eigenvectors $\{\boldsymbol{w}^{(j)}\}$. Indeed,

$$\begin{aligned}(S_k, S_l)_{L^2(\mathcal{C})} &= \frac{1}{\nu_k \nu_l} \int_{\mathcal{C}} \sum_{i=1}^{M} w_i^{(k)} \Phi_i(\boldsymbol{z}') \sum_{j=1}^{M} w_j^{(l)} \Phi_j(\boldsymbol{z}')\, d\boldsymbol{z}' \\ &= \frac{1}{\nu_k \nu_l} \sum_{i=1}^{M} \sum_{j=1}^{M} w_i^{(k)} w_j^{(l)} \int_{\mathcal{C}} \Phi_i(\boldsymbol{z}') \Phi_j(\boldsymbol{z}')\, d\boldsymbol{z}' \\ &= \frac{1}{\nu_k \nu_l} \sum_{i=1}^{M} \sum_{j=1}^{M} w_i^{(k)} w_j^{(l)} \delta_{ij} = \frac{1}{\nu_k \nu_l} \sum_{i=1}^{M} w_i^{(k)} w_i^{(l)} = \frac{1}{\nu_k \nu_l}\, \delta_{kl}.\end{aligned}$$

For the second orthogonality relation we simply use that $\{\nu_l, \boldsymbol{w}^{(l)}\}$ is an eigenpair of the matrix A_{arr} and the orthonormality of the eigenvectors $\{\boldsymbol{w}^{(j)}\}$.

$$\begin{aligned}(S_k, S_l)_{L^2(\mathcal{A})} &= \frac{1}{\nu_k \nu_l} \sum_{i=1}^{M} \sum_{j=1}^{M} w_i^{(k)} w_j^{(l)} \int_{\mathcal{A}} \Phi_i(\boldsymbol{z}') \Phi_j(\boldsymbol{z}')\, d\boldsymbol{z}' \\ &= \frac{1}{\nu_k \nu_l} \sum_{i=1}^{M} w_i^{(k)} \sum_{j=1}^{M} (A_{\text{arr}})_{ij} w_j^{(l)} = \frac{1}{\nu_k \nu_l} \sum_{i=1}^{M} \nu_l\, w_i^{(k)} w_i^{(l)} = \frac{1}{\nu_k}\, \delta_{kl}.\end{aligned}$$

The relation $\frac{\|S_k\|_{L^2(\mathcal{A})}}{\|S_k\|_{L^2(\mathcal{C})}} = \nu_k^{1/2}$ is an immediate consequence of the above two relations. □

In order to illustrate the behavior of the S_j's, we consider the same configuration as in Figure 4, and we plot in Figure 5 the first eight functions $S_j(\boldsymbol{z}')$, $j = 1, 2, \ldots, 8$, for the four different array-types. Here the area of the arrays is approximately equal to $0.04|\mathcal{C}|$, and the corresponding eigenvalues are shown in the last column of Figure 4. For the rectangle and the ellipse the first eight eigenvalues are larger than 0.99, while for the quadrifolium and the annular ellipse they remain above 0.93. As expected in view of Proposition 2, the S_j, for $j = 1, \ldots, 8$, are mainly supported in the interior of the array.

Finally, to provide some idea of the way the S_j behave as j increases, we plot in Figure 6 the functions S_{20} for the same four arrays. Now, the corresponding eigenvalues for the rectangle, the ellipse, the quadrifolium and the annular ellipse are 0.7435, 0.6866, 0.6393 and 0.7049, respectively. We note that, in each case, the values of S_j seem to peak towards the boundary of the array and some oscillations are also visible in the exterior of the array. We have also checked that for larger values of j, that correspond to smaller eigenvalues, the corresponding S_j are mainly supported in the exterior of the array.

Next, we present the proposed algorithms for imaging with planar arrays of general shape that partially cover the waveguide's cross-section.

4.3 Algorithms for imaging with a partial-aperture array

In the case of passive imaging, Algorithm 1 is modified as follows:

Algorithm 3 ***(Passive Imaging – Partial-aperture array)*** *Given the data vector $\Pi(\vec{\boldsymbol{x}}_r)$ and letting S_i, $i = 1, \ldots, M_\varepsilon$, and W_ε be as in Definition 1:*

(a) We construct the $M_\varepsilon \times 1$ vector $\mathbb{S}$ by projecting the recorded field $\Pi(\vec{\boldsymbol{x}}_r)$ onto the M_ε-first functions S_i, $i = 1, \ldots, M_\varepsilon$,

$$\mathbb{S}_i = \int_{\mathcal{A}} \Pi(\vec{\boldsymbol{x}}_r) S_i(\boldsymbol{z}'_r)\, d\boldsymbol{z}'_r, \quad i = 1, \ldots, M_\varepsilon, \tag{23}$$

and we then define the $M \times 1$ vector $\mathbb{Q}$ by

$$\mathbb{Q} = W_\varepsilon\, \mathbb{S}. \tag{24}$$

(b) For each $\vec{\boldsymbol{y}}^{\,\mathrm{s}} \in \mathcal{S}$ we compute the imaging functional given in (14) *and we graphically display the modulus of these values.*

In the case of active imaging, Algorithm 2 takes the form:

Algorithm 4 ***(Active Imaging – Partial-aperture array)***
Given the $N \times N$ array response matrix Π and letting S_i, $i = 1, \ldots, M_\varepsilon$, and W_ε be as in Definition 1:

(a) We compute the $M \times M$ projected matrix $\mathbb{Q}$ as follows:

First, we construct the $M_\varepsilon \times M_\varepsilon$ matrix $\mathbb{S}$ with entries

$$\mathbb{S}_{ij} = \int_{\mathcal{A}} \int_{\mathcal{A}} \Pi(\vec{\boldsymbol{x}}_r, \vec{\boldsymbol{x}}_s) S_i(\boldsymbol{z}'_s) S_j(\boldsymbol{z}'_r)\, d\boldsymbol{z}'_s\, d\boldsymbol{z}'_r, \quad i, j = 1, \ldots, M_\varepsilon, \tag{25}$$

and, then the $M \times M$ matrix $\mathbb{Q}$ by

$$\mathbb{Q} = W_\varepsilon\, \mathbb{S}\, W_\varepsilon^T. \tag{26}$$

(b) For each $\vec{\boldsymbol{y}}^{\,\mathrm{s}} \in \mathcal{S}$ we compute the imaging functional given in (17) *and we graphically display the modulus of these values.*

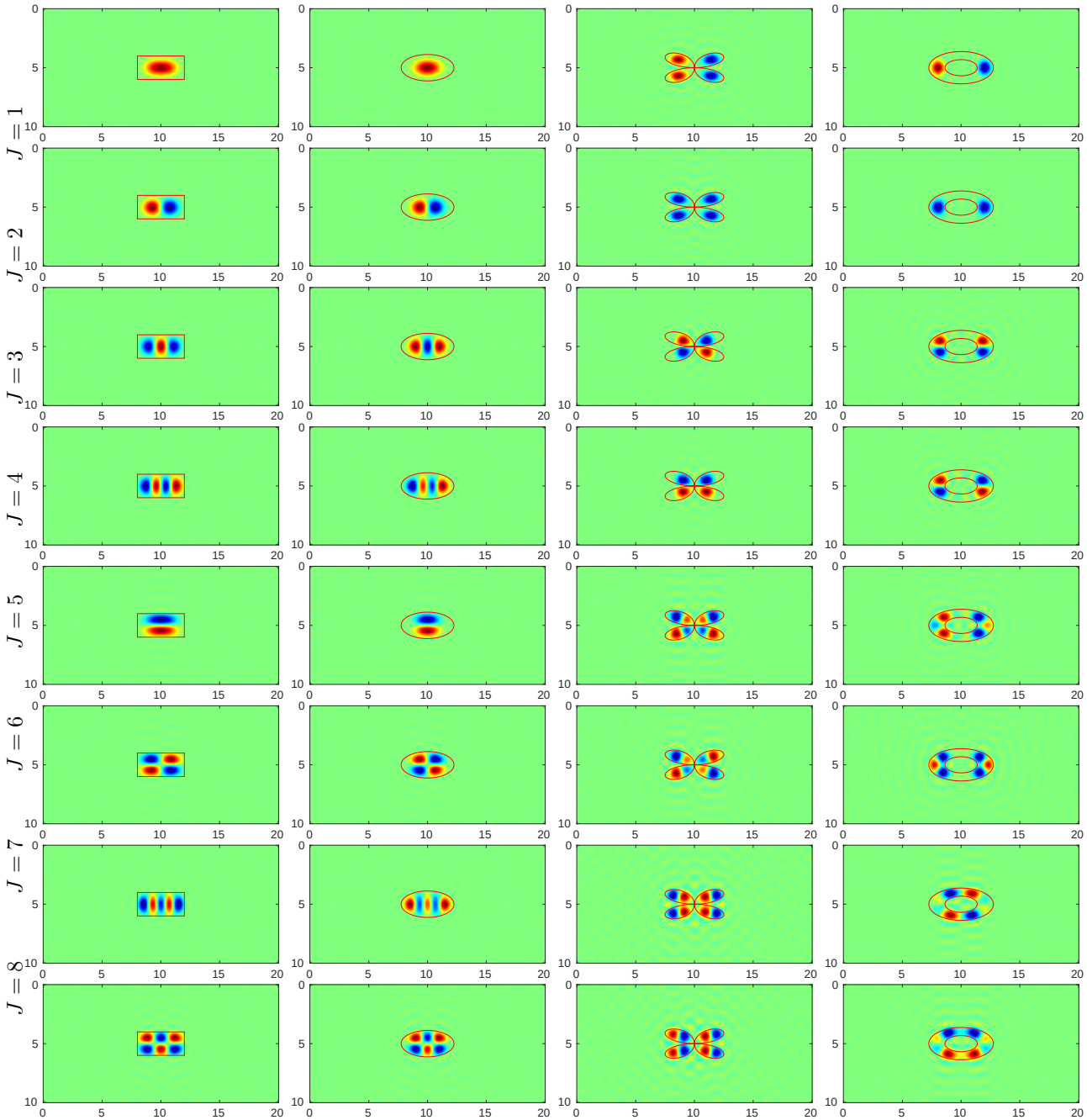

Figure 5: Top to bottom: The first eight functions $S_j(\boldsymbol{z}')$, $j = 1, \ldots, 8$, for the four arrays, i.e. (from left to right) the rectangle, the ellipse, the quadrifolium and the annular ellipse. In all cases $|\mathcal{A}| \approx 0.04|\mathcal{C}|$.

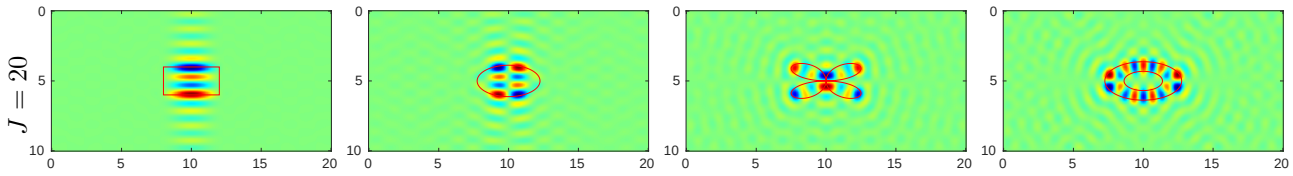

Figure 6: Left to right: The function $S_{20}(\boldsymbol{z}')$ for arrays that have the shape of a rectangle, an ellipse, a quadrifolium and an annular ellipse. In all cases $|\mathcal{A}| \approx 0.04|\mathcal{C}|$.

Let us note that in the full array case ($\mathcal{A} \equiv \mathcal{C}$) the Φ_j are orthonormal along $\mathcal{A}$, hence A_{arr} is just the identity matrix, $S_j = \Phi_j$ and, as a result, the projected response matrix $\mathbb{Q}$ is the same as in (13) and (16) for the passive and the active case, respectively. Thus, in practice, we always use Algorithms 3 and 4 for imaging, setting aside if the array is full or partial.

Moreover, notice that we use the same algorithms for both waveguide geometries, i.e. the terminating and the infinite waveguide. Of course, in the infinite waveguide it is no longer true that the point spread function is determined by the imaginary part of the Green's function. In other words, results (12) and (18) that we have obtained for the terminating case do not hold in the infinite waveguide. (These results may be proven true if we consider an additional full-aperture array located in Ω_{L^+}.) However, a numerical investigation of the point spread function, and all the numerical experiments that we have performed, confirm that this imaging functional provides good reconstructions of the size and the shape of the scatterer when a single array is used in the infinite waveguide. Some of these results will be presented in Section 5.

We close this section with some important observations concerning these imaging algorithms.

4.4 Partial aperture imaging properties.

Assuming the linearized Born approximation for the scattered field, we can show that the image that we obtain with a partial-aperture array is the same as the one derived with a full-aperture array as long as all the eigenvalues ν_j of the matrix A_{arr} are positive. To see this, let us consider a single point scatterer of unit reflectivity that is located in a terminating waveguide Ω^{t}, say at $\vec{\boldsymbol{x}}_* = (z_*, \boldsymbol{z}'_*) \in \Omega_{L^+}$. Moreover, we assume that all the eigenvalues ν_j of the matrix A_{arr} are positive, thus allowing us to consider that $M_\varepsilon = M$ and $W_\varepsilon = W$. Finally, let the array $\mathcal{A}$ be located at range $z = z_a \ll L$, so that the evanescent part of the wave field may be neglected. Then it is quite easy to prove that the projected array response matrix $\mathbb{Q}$ defined by (25) and (26) for a partial aperture array is equal to the projected matrix $\mathbb{Q}$ for an array that spans the entire cross-section $\mathcal{C}$. The proof relies on the fact that the Green's function $G(\vec{\boldsymbol{x}}, \vec{\boldsymbol{x}}_*)$ for a point $\vec{\boldsymbol{x}} = (z, \boldsymbol{z}') \in \Omega_{L^-}$ may be approximated by a linear combination of the first M eigenfunctions $\Phi_i(\boldsymbol{z}')$, $i = 1, \ldots, M$, on the easily derived property

$$\int_{\mathcal{A}} S_k(\boldsymbol{z}')\, \Phi_m(\boldsymbol{z}')\, d\boldsymbol{z}' = w_m^{(k)}, \tag{27}$$

and on the orthogonality of the matrix W. The extension of the proof from the two-dimensional (see Proposition 3.4 in Ref. [28]) to the three-dimensional case is immediate. This is also true for an extended scatterer under the Born approximation as in this case the field can be written as a superposition of point scatterers' fields.

However, this result holds only in an ideal setting, e.g. under the hypothesis of a continuous array and assuming that our computations are 'exact', i.e. they are performed with infinite precision. As we observed in the two-dimensional waveguide, [27] in practice the result remains true only for arrays that cover at least 50% of

the waveguide's cross section while in three dimensions our results suggest (see Section 5, Figure 9) that we need an array that covers approximately 70% of the waveguide. This is because, as the array aperture decreases, the minimum eigenvalue of A_{arr} tends to zero, which leads to numerical instabilities. To counter this phenomenon, in our computations we take into account the eigenvalues ν_i of A_{arr} that stay above a certain threshold ε and, consequently, we use only the first M_ε functions $S_j(\boldsymbol{z}')$ and the $M \times M_\varepsilon$ matrix W_ε. This leads to a low-rank approximation of the full array version of $\mathbb{Q}$, which affects the quality of the image that deteriorates compared to the full aperture case as M_ε decreases.

5 Imaging results

In this section, we asses the effectiveness of our active imaging functional $\mathcal{I}^{\text{a}}$ with numerical experiments. We consider both the full and the partial array-aperture cases for a homogeneous waveguide that forms an infinite or a terminating rectangular parallelepiped, as shown in Figure 7. Different array geometries are considered, such as the ones shown in Figure 4. Regarding the scatterer geometry, we examine three cases: a point scatterer, a two-dimensional square perfect reflector, i.e. a 'screen' that is perpendicular to the waveguide axis, and a hemispherical scatterer.

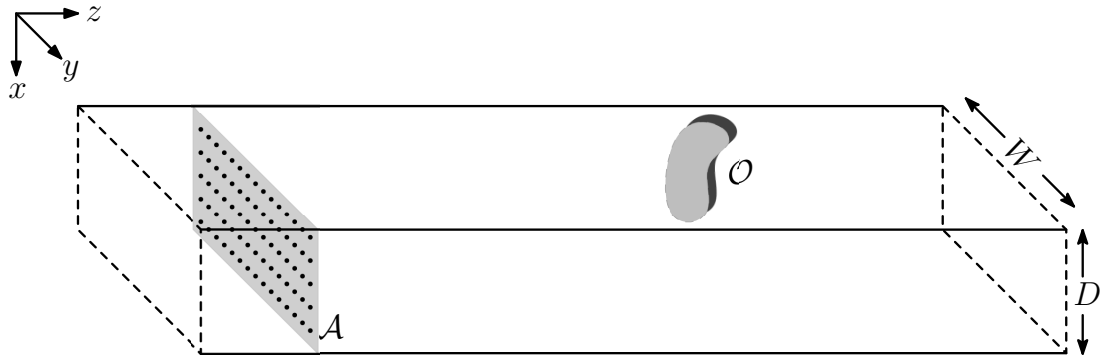

Figure 7: Schematic representation of the active imaging problem in a parallepiped waveguide.

Using the single scattering Born approximation and denoting by $\mathcal{O}$ the domain occupied by the scatterer, the array response matrix Π takes the form

$$\Pi(\vec{\boldsymbol{x}}_s, \vec{\boldsymbol{x}}_r; \omega) = \int_{\mathcal{O}} G(\vec{\boldsymbol{x}}_s, \vec{\boldsymbol{x}}; \omega) G(\vec{\boldsymbol{x}}, \vec{\boldsymbol{x}}_r; \omega)\, d\vec{\boldsymbol{x}}, \tag{28}$$

where we omitted the (multiplicative) constant wavenumber k^2. We use (28) to compute the data for the three different scatterer geometries. For the Green's function in (28) we use the analytical expression (32) for the infinite waveguide case and (33) for the terminating one that are given in Appendix A. For a more general waveguide geometry or for an inhomogeneous medium, the Green's function and the array response matrix should be computed numerically.

The image is obtained by displaying the values of the imaging functional $\mathcal{I}^{\text{a}}$ for points $\vec{\boldsymbol{y}}^{\text{S}}$ in the search domain $\mathcal{S}$,

$$\mathcal{I}^{\text{a}}(\vec{\boldsymbol{y}}^{\text{S}}) = \sum_{i=1}^{M} \sum_{j=1}^{M} \beta_i\ \beta_j\ \overline{\mathbb{Q}_{ij}}\ G_i(z_a, \vec{\boldsymbol{y}}^{\text{S}})\ G_j(z_a, \vec{\boldsymbol{y}}^{\text{S}}). \tag{29}$$

Here $\mathbb{Q}$ is the projected array response matrix (see (16) for the full-aperture case and Equations (25) and (26) for the partial-aperture) and G_i is as in Equation (9).

We also introduce the multiple-frequency version of $\mathcal{I}^{\text{a}}$, which is derived from (29) by summing over frequency, i.e.

$$\mathcal{I}^{\text{a}}(\vec{\boldsymbol{y}}^{\text{s}}) = \sum_{l=1}^{N_f} \sum_{i=1}^{M_l} \sum_{j=1}^{M_l} \beta_i(f_l)\ \beta_j(f_l)\ \overline{\mathbb{Q}_{ij}(f_l)}\ G_i(z_a, \vec{\boldsymbol{y}}^{\text{s}}, f_l)\ G_j(z_a, \vec{\boldsymbol{y}}^{\text{s}}, f_l), \tag{30}$$

where f_l, $l = 1, \ldots, N_f$, are the discrete frequencies that span the available frequency interval $[f_{\min}, f_{\max}]$ in our data. Note that M_l depends on the index l since the number of propagating modes depends on the frequency f_l.

In all following test cases the waveguide cross-section is $\mathcal{C} = [0, D] \times [0, W]$ and has dimensions $D = 10\lambda_0$ and $W = 20\lambda_0$, where λ_0 is the reference wavelength corresponding to the reference wavenumber $k_0 = \pi/10$. Whenever we consider a single frequency it refers to the wavenumber $k = 0.9875k_0$. The array is always placed perpendicular to the waveguide axis at range $z_a = 0$, and the inter-element lattice parameter h is taken equal to $h = \lambda_0/8$. In the case of the terminating waveguide, the terminating vertical boundary is placed at range $R = 28\lambda_0$. Finally, the search domain $\mathcal{S}$ is a box with zxy-dimensions $[17, 21] \times [3, 7] \times [8, 12]$, in terms of λ_0.

Test case 1: A point scatterer

In our first test case we consider a single point scatterer located at $\vec{\boldsymbol{x}}_* = (19, 5, 10)\lambda_0$. We use a rectangular array that spans the entire cross-section (full array-aperture) and consists of $N = 13041$ transducers that emit at a single frequency. The entries of the $N \times N$ array response matrix Π are given in (15).

In Figure 8 we plot the modulus of $\mathcal{I}^{\text{a}}$, for the infinite waveguide in the left subplot and for the terminating in the right one. Each image is normalized by the maximum value of the modulus of $\mathcal{I}^{\text{a}}$ and, moreover, we only display the values of $\mathcal{I}^{\text{a}}$ with modulus larger than a threshold ℓ, which in this case is chosen as $\ell = 0.5$. We use this thresholding process to display the large values of the imaging functional that contain information about the scatterer. This parameter ℓ is chosen on a case by case basis and will be specified separately in each example. We also plot the projections of the image on z, x and y-planes with a gray 'shadow' color. Note that these two images of the point scatterer in the case of an infinite and a terminating waveguide, respectively, are in fact depicting the graph of the so-called point spread function (PSF) for the imaging functional $\mathcal{I}^{\text{a}}$ in each case.

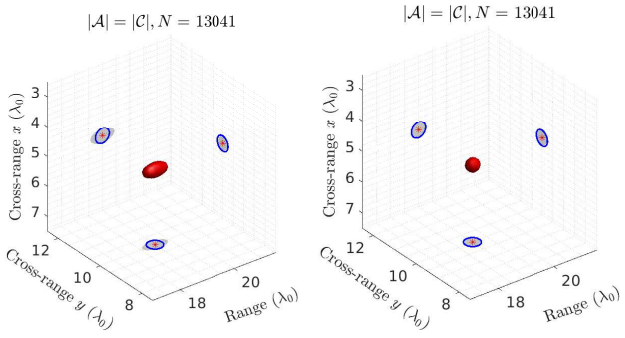

Figure 8: Imaging a point scatterer located at $\vec{\boldsymbol{x}}_* = (19, 5, 10)\lambda_0$ with $\mathcal{I}^{\text{a}}$, for the full array case for the infinite waveguide (left) and the terminating waveguide with $R = 28\lambda_0$ (right) for a single frequency with $k = 0.9875k_0$. Here, the threshold $\ell = 0.5$.

In both images in Figure 8 the scatterer is located with very good accuracy. Note that the image that is shown on the right, which corresponds to the terminating waveguide, exhibits better resolution in range compared to its counterpart for the infinite waveguide. In fact, using (18), we can prove that the resolution of $\mathcal{I}^{\text{a}}$ in the terminating waveguide is equal to $\lambda/2$ in all directions, where λ is the wavelength that corresponds

to the frequency that we use. For a detailed proof of this result in the case of a two-dimensional waveguide, we refer to Ref. [28]. Here, we define the resolution of the image as the width of the main lobe at its half-height (hence the choice of $\ell = 0.5$), and is indicated in our plots with a circle, typed in blue, of diameter $\lambda/2$ that is drawn on each plane and is centered at the projection of the true location of the point scatterer on each plane.

Test case 2: A screen parallel to the array

Next, we consider a two-dimensional square perfect reflector, a 'screen', that is placed in an infinite waveguide parallel to its cross-section. The square scatterer has sidelength $b = 2\lambda_0$ and is centered at $\vec{\boldsymbol{x}}_* = (19, 5, 10)\lambda_0$. In this test case we shall experiment with arrays of various partial apertures, with arrays of different shapes, and we shall also demonstrate the benefit of using multiple frequencies.

Furthermore, in order to assess the performance of our imaging functional $\mathcal{I}^{\mathrm{a}}$ under the presence of measurement noise, we add to the response matrix $\Pi(\omega)$ a noise matrix $W(\omega)$ with zero mean uncorrelated Gaussian distributed entries with variance $\epsilon p_{\mathrm{avg}}$. Here the average power received per source, receiver and frequency is given by

$$p_{\mathrm{avg}} = \frac{1}{N^2 N_f} \sum_{i=1}^{N_f} \|\Pi(\omega_i)\|_{\mathrm{F}}^2,$$

where $\|\cdot\|_{\mathrm{F}}$ is the Frobenius matrix norm. Then, the normalized noise power in dB is $-10\log_{10}\epsilon$. Specifically, in all results that we are going to show next for the screen scatterer, we assume a level of additive noise of 10 dB.

Imaging with partial-aperture arrays – Single frequency. We first start with a single frequency ($k = 0.9875k_0$) that corresponds to $M = 584$ propagating modes, and with a rectangular array that covers the entire cross-section $\mathcal{C}$. Then, we gradually decrease the area of the rectangular array keeping it always centered with respect to the cross-section $\mathcal{C}$. To be more specific, we remove array elements from the edges of the array and, since $W = 2D$, we remove twice as many transducers in the y-direction than in x.

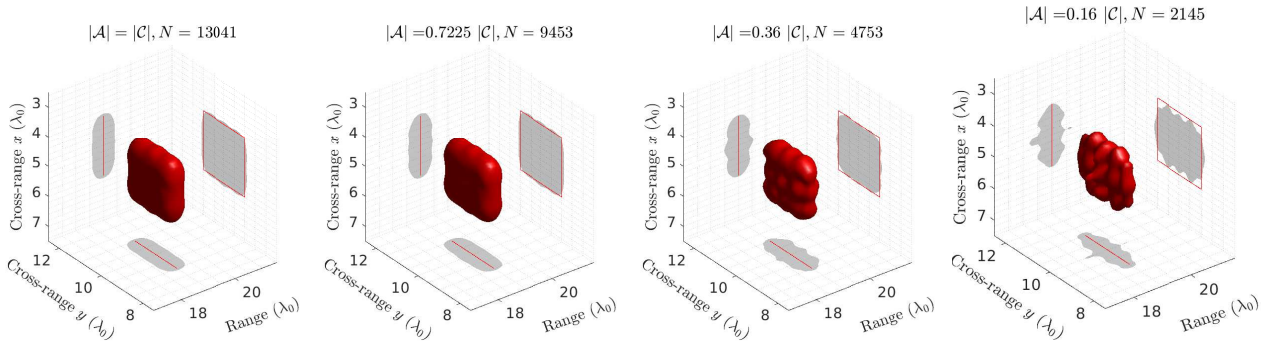

Figure 9: Imaging a vertical square screen of sidelength $b = 2\lambda_0$, centered at $\vec{\boldsymbol{x}}_* = (19, 5, 10)\lambda_0$ with $\mathcal{I}^{\mathrm{a}}$ for the full array case (left) and for centered rectangular arrays with $|\mathcal{A}| = 0.7225, 0.36, 0.16\,|\mathcal{C}|$ for a single frequency with $k = 0.9875k_0$ for 10 dB noise. Here, $\ell = 0.15$.

In Figure 9 we present four images created with $\mathcal{I}^{\mathrm{a}}$ that correspond, from left to right, to arrays that satisfy: a) $|\mathcal{A}| = |\mathcal{C}|$ (full array-aperture), b) $|\mathcal{A}| \approx 0.72|\mathcal{C}|$, c) $|\mathcal{A}| = 0.36|\mathcal{C}|$, and d) $|\mathcal{A}| = 0.16|\mathcal{C}|$, respectively. In each subplot we depict the three-dimensional reconstruction of the scatterer and its projection on all planes. The projection of the actual boundary of the screen on each plane is indicated with a red line. As one may immediately verify, the first two images that correspond to the full array-aperture and to the array that covers approximately 72% of $|\mathcal{C}|$, look almost identical. The value of the threshold ε is 10^{-6} while for $|\mathcal{A}| \approx 0.72|\mathcal{C}|$

the minimum eigenvalue of $A_{\rm arr}$ is equal to $\mu_{\min} = 1.15 \cdot 10^{-5}$. Consequently, the number M_ε (see Definition 1) of functions S_j that are employed in the construction of the $M \times M$ projected response matrix $\mathbb{Q}$ (see (25) and (26)) is taken equal to $M = 584$. Then, as expected in view of the discussion below Equation (27), we do not lose any information compared to the full-aperture case.

For the third and fourth images in Figure 9 that correspond to arrays that cover 36% and 16% of $|\mathcal{C}|$, respectively, it turns out that some eigenvalues of the matrix $A_{\rm arr}$ fall below the threshold ε resulting to $M_\varepsilon = 403$ and 225, respectively. This low rank approximation of the full array-aperture version of the projected matrix $\mathbb{Q}$ leads to images with lower quality than the previous ones. However, even the fourth image in Figure 9 still provides good estimates of the location and the shape of the screen, given the fact that we illuminate the scatterer with a single frequency and we use an array that covers just 16% of the area of the original array. In terms of number of transducers, the array in the fourth image contains 2145 transducers compared to 13041 transducers that are supported in the full array aperture case.

Imaging with arrays of different shapes – Single frequency. Next, we shall use arrays of different shapes in order to check whether, and in what extent, the shape of the array affects the $\mathcal{I}^{\rm a}$ image. Specifically, we have experimented with the four array shapes that we have already introduced, see Figure 4, namely a rectangle, an ellipse, a quadrifolium and an annular ellipse. Here we shall present our results for arrays that cover approximately 40% of $|\mathcal{C}|$ and for a single frequency. In the top row of Figure 10 the gray area indicates the part of the cross-section $\mathcal{C}$ that each array covers, while in the bottom row we may see the associated three-dimensional reconstructions of the screen.

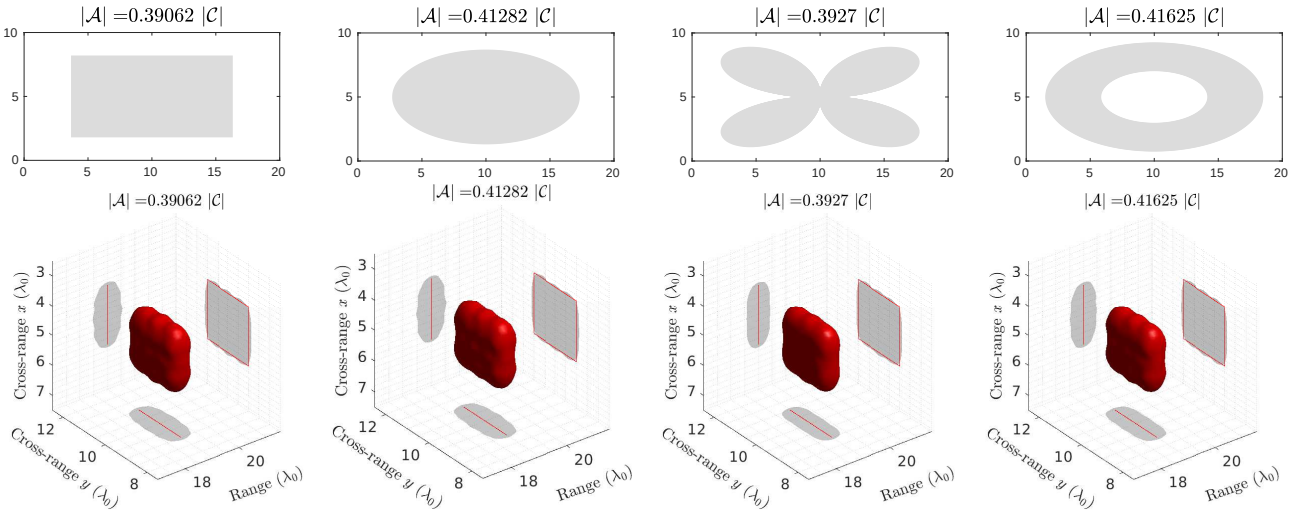

Figure 10: Top: Array shape. Bottom: Image of a square screen of sidelength $b = 2\lambda_0$, centered at $\vec{\boldsymbol{x}}_* = (19, 5, 10)\lambda_0$ with $\mathcal{I}^{\rm a}$ for $|\mathcal{A}| \simeq 0.4\ |\mathcal{C}|$, for a single frequency with $k = 0.9875 k_0$ for 10 dB noise. Here, $\ell = 0.15$. Array shape from left to right: Rectangle, ellipse, quadrifolium and annular ellipse.

These images, as well as other tests that we have performed with these four array types, indicate that arrays of different shape that occupy approximately the same area furnish very similar $\mathcal{I}^{\rm a}$ images.

Using multiple frequencies. A way to improve the quality of an image, especially when we use arrays with small aperture, is to use multiple frequencies to illuminate the reflector. In Figure 11 we present multiple frequency results for imaging with $\mathcal{I}^{\rm a}$. Specifically, the central frequency f_c corresponds to the wavenumber $k_c = 0.9875\, k_0$ and we use frequencies $f \in [f_c - B/2, f_c + B/2]$, where B denotes the bandwidth, which we take

it here equal to $B \simeq 0.92 f_c$. On the leftmost plot, we present the $\mathcal{I}^{\text{a}}$ image for a rectangular array (centered to the cross-section $\mathcal{C}$) with $|\mathcal{A}| = 0.16|\mathcal{C}|$. It is immediate to see a clear improvement in the quality of the image when we compare it with the rightmost image of Figure 9 which was created with the same array aperture but with a single frequency illumination. The three other images in Figure 11 correspond, from left to right, to centered rectangular arrays that cover an area $|\mathcal{A}|$ equal to 0.1225, 0.09 and 0.04 of $|\mathcal{C}|$, respectively. Although, as expected, the image does deteriorate as the array aperture decreases, we observe that reliable information about the location, size and shape of the scatterer is obtained in all cases. It is worth noting that we are still able to create a meaningful image by using only 4% of the original array, which is translated to 561 out of 13041 transducers.

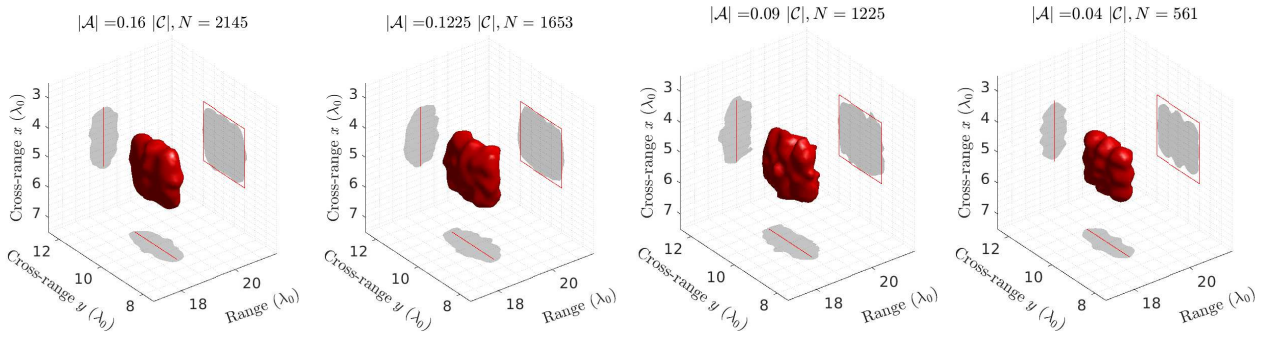

Figure 11: Imaging a vertical square screen of sidelength $b = 2\lambda_0$, centered at $\vec{\boldsymbol{x}}_* = (19, 5, 10)\lambda_0$ with $\mathcal{I}^{\text{a}}$ for $|\mathcal{A}| = 0.16, 0.1225, 0.09, 0.04|\mathcal{C}|$ for frequencies with $k \in [0.5375, 1.4375]k_0$, for 10 dB noise. Here, $\ell = 0.45$.

Test case 3: A hemispherical scatterer

Lastly, we examine the more challenging case of a hemispherical scatterer that faces the array. The scatterer has diameter $b = 2\lambda_0$ and is centered at $\vec{\boldsymbol{x}}_* = (19, 5, 10)\lambda_0$. In Figure 12 we show $\mathcal{I}^{\text{a}}$ images for a full array-aperture and a single frequency. The image on the left concerns the infinite waveguide case, while the one on the right the terminating waveguide. As in the previous test cases, the projection of the true boundary of the scatterer on each plane is marked with a red line. It is immediate to see that the image for the infinite waveguide, on the left hand-side, is focused mainly on the leftmost part of the scatterer. On the other hand, the image for the terminating waveguide on the right, provides a better estimate of the scatterer's support. We may attribute this improvement to the multiple reflections that bounce off the terminating boundary and provide us with diverse views of the scatterer which are not attainable in the infinite waveguide case.

Next, to follow on from the results that we have presented for the square screen scatterer, we examine the behavior of our imaging functional as the array aperture decreases. In Figure 13 we consider arrays with areas equal to $|\mathcal{A}| = 0.72,\ 0.36,\ 0.16\ |\mathcal{C}|$. We observe that for $|\mathcal{A}| = 0.72|\mathcal{C}|$ the image looks virtually unchanged compared to the full array case (right subplot in Figure 12). As we have already discussed in the previous test case, for the given array aperture we use all $M = 584$, S_j functions in order to compute the projected response matrix $\mathbb{Q}$. However, as we decrease the array further we need to consider $M_\varepsilon < M$, and the quality of the image deteriorates, as expected. For $|\mathcal{A}| = 0.36|\mathcal{C}|$ the image is more noisy but it still retains good information about the location and the shape of the scatterer. For $|\mathcal{A}| = 0.16|\mathcal{C}|$ we can still extract information about the location of the scatterer, but the recovered shape is quite distorted.

As we have seen in Test case 2, we may use multiple frequencies in order to improve the quality of the image. As before, we use a central frequency f_c with wavenumber $k_c = 0.9875k_0$ and a bandwidth $B \simeq 0.92 f_c$. Now, the image for $|\mathcal{A}| = 0.16|\mathcal{C}|$, shown in the leftmost subplot in Figure 14 manifests a significant improvement compared to its single-frequency counterpart that is shown in the rightmost subplot in Figure 13. Now, we can

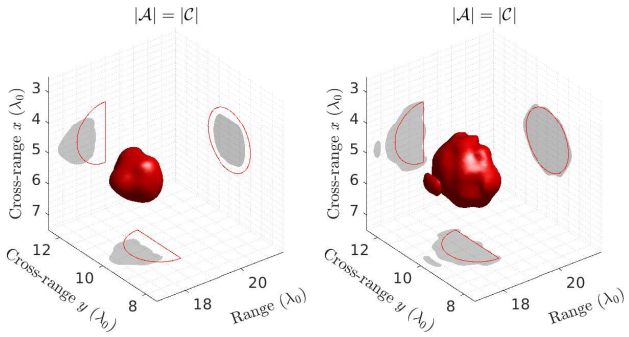

Figure 12: Imaging a hemispherical scatterer of diameter $b = 2\lambda_0$, centered at $\vec{\boldsymbol{x}}_* = (19, 5, 10)\lambda_0$, with $\mathcal{I}^{\text{a}}$ for the full array case for the infinite (left) and the terminating waveguide (right), for a single frequency with $k = 0.9875k_0$ and $R = 28\lambda_0$. Here, $\ell = 0.18$.

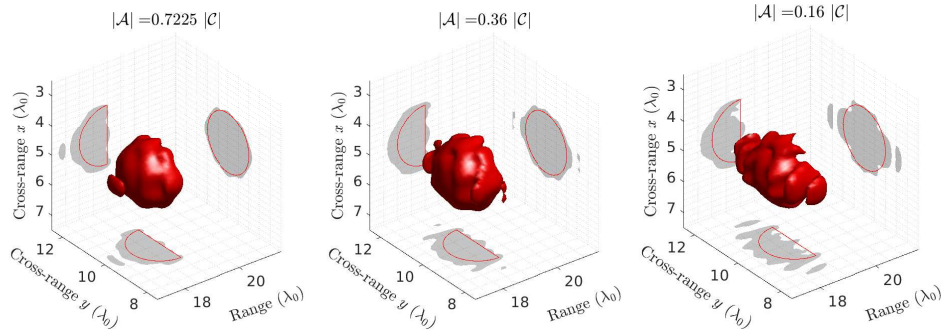

Figure 13: Imaging a hemispherical scatterer of diameter $b = 2\lambda_0$, centered at $\vec{\boldsymbol{x}}_* = (19, 5, 10)\lambda_0$, with $\mathcal{I}^{\text{a}}$ for $|\mathcal{A}| = 0.72, 0.36, 0.16\ |\mathcal{C}|$ for a single frequency with $k = 0.9875k_0$ and $R = 28\lambda_0$. Here, $\ell = 0.18$.

decrease the array size even more to $|\mathcal{A}| \approx 0.12,\ 0.09,\ 0.04\ |\mathcal{C}|$, and the corresponding images that are shown in Figure 14 are still meaningful, in the sense that they provide information mainly about the location and the size and, to a lower extent, about the shape of the scatterer.

To summarize, in this section we have presented imaging results for various scatterer and array geometries, with data that were generated by the Born approximation, in order to assess the performance of our imaging method. We first examined the PSF of our imaging functional in the case of an infinite and a terminating waveguide that forms a rectangular parallelepiped. The other two test cases concerned extended reflectors and, specifically, a screen and a hemisphere. We have experimented with various array sizes and shapes, with single and multiple frequencies, and in the case of the screen we presented imaging results under the presence of 10 dB measurement noise.

For a single frequency, we have seen that as long as the array covers a significant part of the waveguide's cross-section (in our experiments approximately 75%), then the images that we get are almost the same with those obtained with a full array-aperture. As the size of the array decreases the quality of the image deteriorates. However, images that were created with arrays that covered approximately 16% of the waveguide's cross-section still provided useful information about the position and the shape of the scatterer.

The use of multiple frequencies greatly improved the effectiveness of our method allowing us to create good images with arrays that covered approximately 5% of the waveguide's cross-section. In the case of the hemispherical scatterer we have observed a benefit of imaging in a terminating waveguide, in the sense that we were able to fully reconstruct the shape of the scatterer by taking advantage of the multiple reflections due to the presence of a 'wall' behind the obstacle. Finally, our tests indicate that arrays of different shape that cover

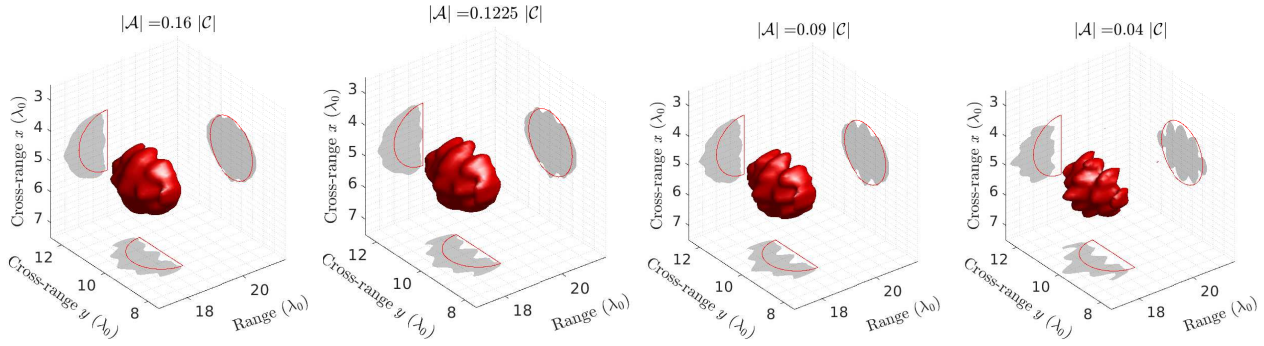

Figure 14: Imaging a hemispherical scatterer of diameter $b = 2\lambda_0$, centered at $\vec{\boldsymbol{x}}_* = (19, 5, 10)\lambda_0$, with $\mathcal{I}^{\text{a}}$ for $|\mathcal{A}| = 0.16, 0.1225, 0.09, 0.04\ |\mathcal{C}|$ for frequencies with $k \in [0.5375, 1.4375]k_0$ and $R = 28\lambda_0$. Here $\ell = 0.2$.

approximately the same area, and have the same element density, produce similar images.

6 Concluding Remarks

In this paper, we studied the problem of imaging extended reflectors embedded in three-dimensional waveguides, using an active planar array that is parallel to the waveguide's cross-section and may span its entirety or part of it. We considered two cases, as far as the waveguide geometry is concerned: the *infinite* waveguide, which allows waves to travel infinitely in both directions in range and the *terminating* waveguide, where, we assume that there is an additional boundary on the right side of the waveguide, and consequently waves are only allowed to propagate infinitely on the left side.

For both geometries, we use an imaging functional that relies on the back-propagation of a projection of the array response matrix on the propagating modes. The main contribution of this paper is the definition of the projection operator for arrays that partially cover the waveguide's cross-section. This projection hinges upon defining a finite-dimensional subspace of functions that are orthogonal along both the array and the waveguide cross-section and exhibit maximum fractional concentration of energy in the array aperture.

Our imaging results illustrate that good reconstructions of extended scatterers are obtained for arrays occupying a very small fraction of the waveguide cross-section, even for single-frequency illumination. The use of multiple frequencies allows us to decrease the size of the array even further. We have also observed that the reconstructions are better in the terminating waveguide compared to the infinite waveguide case. This is intuitively expected, since in the terminating waveguide there exist multiple-scattering paths between the scatterer and the terminating boundary, which provide us with more information about the reflector.

Acknowledgments

The work of C. Tsogka was partially supported by AFOSR FA9550-17-1-0238 and AFOSR FA9550-18-1-0519. The work of S. Papadimitropoulos was supported by the Fund for the Promotion of Research at the Technion. This work has been initiated while the authors were in residence at the Institute for Computational and Experimental Research in Mathematics (ICERM) in Providence, RI, during the Fall 2017 semester (National Science Foundation, Grant No. DMS-1439786). The inspiring ICERM/Brown University research environment and its kind hospitality are warmly acknowledged.

A The Green's function for a homogeneous waveguide with a rectangular transverse profile

In this appendix we present the Green's functions for an infinite and a terminating homogeneous waveguide with transverse profile the rectangle $\mathcal{C} = [0, D] \times [0, W]$. Specifically, we consider the infinite waveguide $\Omega^{\mathrm{i}} = \mathbb{R} \times \mathcal{C}$ and the terminating one $\Omega^{\mathrm{t}} = (-\infty, R] \times \mathcal{C}$. The range variable along the waveguide axis is z, and the cross-range coordinates are $\boldsymbol{z}' = (x, y) \in \mathcal{C}$. The Green's function due to a point source at $\vec{\boldsymbol{x}}_s = (z_s, \boldsymbol{z}'_s)$, for a single frequency ω, solves the problem

$$\begin{cases} -\Delta G(\vec{\boldsymbol{x}}, \vec{\boldsymbol{x}}_s; \omega) - k^2 G(\vec{\boldsymbol{x}}, \vec{\boldsymbol{x}}_s; \omega) = \delta(\vec{\boldsymbol{x}} - \vec{\boldsymbol{x}}_s), \quad \vec{\boldsymbol{x}} \in \Omega, \\ G(\vec{\boldsymbol{x}}, \vec{\boldsymbol{x}}_s; \omega) = 0, \quad \vec{\boldsymbol{x}} \in \partial\Omega, \end{cases}$$

where $k = \omega/c_0$ is the constant (real) wavenumber, and $\Omega = \Omega^{\mathrm{i}}$ (or Ω^{t}) in the case of the infinite (or terminating) waveguide.

The simple geometry of the waveguide allows us to write explicitly the Green's function in terms of the eigenfunctions of the negative transverse Dirichlet Laplacian in $\mathcal{C}$, i.e.

$$\begin{aligned} -\Delta_{\boldsymbol{z}'} \Phi &= \mu \, \Phi \quad \text{in } \mathcal{C} = [0, D] \times [0, W], \\ \Phi &= 0 \quad \text{on } \partial\mathcal{C}, \end{aligned} \tag{31}$$

see also (3). We have discussed the properties of the eigenvalues μ_n and corresponding eigenfunctions Φ_n in Section 2 (right after (3)).

Then the Green's function in the case of the infinite waveguide[16] Ω^{i} is written as

$$G(\vec{\boldsymbol{x}}, \vec{\boldsymbol{x}}_s; \omega) = \frac{i}{2} \sum_{m=1}^{\infty} \frac{\mathrm{e}^{i\beta_m |z - z_s|}}{\beta_m} \Phi_m(\boldsymbol{z}') \Phi_m(\boldsymbol{z}'_s), \tag{32}$$

while in the case of the terminating waveguide[28] Ω^{t} reads

$$G(\vec{\boldsymbol{x}}, \vec{\boldsymbol{x}}_s; \omega) = \frac{i}{2} \sum_{m=1}^{\infty} \frac{\mathrm{e}^{i\beta_m |z - z_s|} - \mathrm{e}^{i\beta_m |z + z_s - 2R|}}{\beta_m} \Phi_m(\boldsymbol{z}') \Phi_m(\boldsymbol{z}'_s). \tag{33}$$

In (32) and (33), β_n are the horizontal wavenumbers that we have defined in (4).

Moreover, since $\mathcal{C}$ is a rectangle we are able to derive analytically the eigenpairs (μ_n, Φ_n). Separating the cross-range variables x, y in (31), we end up with the two following one-dimensional eigenvalue problems:

$$\begin{cases} X''(x) + \kappa X(x) = 0 \text{ in } [0, D], \\ X(0) = X(D) = 0, \end{cases} \quad \text{and} \quad \begin{cases} Y''(y) + \lambda Y(y) = 0 \text{ in } [0, W], \\ Y(0) = Y(W) = 0. \end{cases} \tag{34}$$

Then the eigenvalues and corresponding orthonormal eigenfunctions are given by

$$\kappa_n = \frac{n^2 \pi^2}{D^2}, \quad X_n(x) = \sqrt{\frac{2}{D}} \sin \sqrt{\kappa_n} x, \quad \text{and} \quad \lambda_n = \frac{n^2 \pi^2}{W^2}, \quad Y_n(y) = \sqrt{\frac{2}{W}} \sin \sqrt{\lambda_n} y. \tag{35}$$

Hence the eigenpairs (μ_n, Φ_n) of (31) are:

$$\mu_n = \mu_{(l,m)} = \kappa_l + \lambda_m = \left(\frac{l^2}{D^2} + \frac{m^2}{W^2} \right) \pi^2, \quad \Phi_n(\boldsymbol{z}') = \Phi_{(l,m)}(x, y) = X_l(x) Y_m(y), \tag{36}$$

where n is the double-index (l, m).

Let us remark that although the eigenvalues of the one-dimensional problems (34) are simple, the eigenvalues of the two-dimensional problem (31) may be degenerate (not simple) in the case where the ratio $(D/W)^2$ is rational.[11] An eigenfunction that corresponds to a degenerate eigenvalue is a linear combination of the

associated functions. For example, in the waveguide with the rectangular cross-section that we have considered for our numerical experiments in Section 5, where $W = 2D$ we have, e.g., that $\mu_{(2,2)} = \mu_{(1,4)}$.

We close this section with some comments on the number M of propagating modes in the previously described waveguide. M is equal to the number of eigenvalues μ_n that are less than $k^2 = (2\pi/\lambda)^2$, where λ is the wavelength that corresponds to the constant wavenumber k. Hence,

$$\begin{aligned} \mu_n = \mu_{(l,m)} < k^2 \Leftrightarrow \left(\frac{l^2}{D^2} + \frac{m^2}{W^2}\right)\pi^2 < \left(\frac{2\pi}{\lambda}\right)^2 \\ \Leftrightarrow \frac{l^2}{(2D/\lambda)^2} + \frac{m^2}{(2W/\lambda)^2} < 1. \end{aligned} \tag{37}$$

An estimate of M is given by Weyl's conjecture which in two dimensions states that

$$M = \frac{\mu_2(\mathcal{C})}{4\pi}\, k^2 - \frac{\mu_1(\partial\mathcal{C})}{4\pi}\, k + o(k) \quad (k \to \infty),$$

where $\mu_2(\mathcal{C})$ and $\mu_1(\mathcal{C})$ are the area and perimeter of $\mathcal{C}$, respectively.[11] The second term in this asymptotic representation is not rigorously proved for general domains. However, in our case where $\mathcal{C}$ is the rectangle $[0, D] \times [0, W]$ this results reads

$$M \approx \frac{\pi DW}{\lambda^2} - \frac{D + W}{\lambda}, \tag{38}$$

and may be justified as follows: Consider the lattice $\mathbb{Z}^2$. Then, in view of (37), M is the number of lattice points in the interior of the part of the ellipse with semi-axes $2D/\lambda$ and $2W/\lambda$ which lies in the first quadrant. Number theory results assert that the area of the elliptic sector $(\pi/4)(2D/\lambda)(2W/\lambda)$ is equal to the number M of the lattice points in the elliptic sector plus half the number of the lattice points residing on the straight parts of the boundary of the sector plus an error term of $o(k)$.[24]

For example, in all results shown in Section 5 we assume $D = 10\lambda_0$, $W = 20\lambda_0$ (λ_0 is a reference wavelength) and, in some cases, we consider a single frequency that corresponds to a wavelength λ such that $\lambda_0/\lambda = 0.9875$. With these values the actual number of propagating modes is $M = 584$, while the estimate (38) predicts 583 propagating modes.

References

[1] T. Arens, D. Gintides, and A. Lechleiter. Direct and inverse medium scattering in a three-dimensional homogeneous planar waveguide. *SIAM J. Appl. Math.*, 71(3):753–772, 2011.

[2] M. D. Bedford and G. A. Kennedy. Modeling microwave propagation in natural caves passages. *IEEE Trans. Antennas and Propagation*, 62(12):6463–6471, 2014.

[3] L. Borcea, F. Cakoni, and S. Meng. A direct approach to imaging in a waveguide with perturbed geometry. *J. Comput. Phys.*, 392:556 – 577, 2019.

[4] L. Borcea and S. Meng. Factorization method versus migration imaging in a waveguide. *Inverse Problems*, 2019.

[5] L. Borcea and D.-L. Nguyen. Imaging with electromagnetic waves in terminating waveguides. *Inverse Probl. Imaging*, 10:915–941, 2016.

[6] L. Bourgeois and E. Lunéville. The linear sampling method in a waveguide: a modal formulation. *Inverse problems*, 24(1):015018, 2008.

[7] L. Bourgeois and E. Lunéville. On the use of sampling methods to identify cracks in acoustic waveguides. *Inverse Problems*, 28(10):105011, 2012.

[8] J. L Buchanan, R. P Gilbert, A. Wirgin, and Y. Xu. *Marine acoustics: direct and inverse problems*. Siam, 2004.

[9] V. K. Chillara and C. J. Lissenden, III. Review of nonlinear ultrasonic guided wave nondestructive evaluation: Theory, numerics, and experiments. *Optical Engineering*, 55(1), 1 2016.

[10] S. Dediu and J. R. McLaughlin. Recovering inhomogeneities in a waveguide using eigensystem decomposition. *Inverse Problems*, 22(4):1227–1246, 2006.

[11] Denis S. Grebenkov and B.-T. Nguyen. Geometrical structure of laplacian eigenfunctions. *SIAM Rev.*, 55(4):601–667, 2013.

[12] A. Haack, J. Schreyer, and G. Jackel. Report to ita working group on maintenance and repair of underground structures: State-of-the-art of non-destructive testing methods for determining the state of a tunnel lining. *Tunnelling and Underground Space Technology*, 10(4):413 – 431, 1995.

[13] R. A. Horn and C. R. Johnson. *Matrix Analysis*. Cambridge University Press, New York, NY, USA, 2nd edition, 2012.

[14] M. Ikehata, G. N. Makrakis, and G. Nakamura. Inverse boundary value problem for ocean acoustics using point sources. *Math. Methods Appl. Sci.*, 27(12):1367–1384, 2004.

[15] D. R. Jackson and D. R. Dowling. Phase conjugation in underwater acoustics. *J. Acoust. Soc. Amer.*, 89(1):171–181, 1991.

[16] F.B. Jensen, W.A. Kuperman, M.B. Porter, and H. Schmidt. *Computational Ocean Acoustics*. Modern Acoustics and Signal Processing. Springer, 2011.

[17] W.A. Kuperman and D. Jackson. Ocean acoustics, matched-field processing and phase conjugation. Topics Appl. Phys., pages 43–97. Springer Berlin / Heidelberg, 2002.

[18] P. Monk and V. Selgas. Sampling type methods for an inverse waveguide problem. *Inverse Probl. Imaging*, 6(4):709–747, 2012.

[19] B. Pinçon and K. Ramdani. Selective focusing on small scatterers in acoustic waveguides using time reversal mirrors. *Inverse Problems*, 23:1–25, 2007.

[20] F.J. Podd, M.T.B. Ali, K.V. Horoshenkov, A.S. Wood, S.J. Tait, J.C. Boot, R. Long, and A.J. Saul. Rapid sonic characterisation of sewer change and obstructions. *Water Science and Technology*, 56(11):131–139, 12 2007.

[21] R. P. Porter. Generalized holography as a framework for solving inverse scattering and inverse source problems. Prog. Opt. XXVII. Elsevier, New York, 1989.

[22] C. Prada, J. de Rosny, D. Clorennec, J.-G. Minonzio, A. Aubry, M. Fink, L. Berniere, P. Billand, S. Hibral, and T. Folegot. Experimental detection and focusing in shallow water by decomposition of the time reversal operator. *J. Acoust. Soc. Amer.*, 122:761–768, 2007.

[23] T. Schultz, D. Bowen, G. Unger, and R. H. Lyon. Remote acoustical reconstruction of cave and pipe geometries. *J. Acoust. Soc. Amer.*, 121(5):3155–3155, 2007.

[24] M.A. Sumbatyan and A. Scalia. *Equations of Mathematical Diffraction Theory*. Chapman & Hall/CRC Press, 2005.

[25] A. Tolstoy, K.V. Horoshenkov, and M.T. Bin Ali. Detecting pipe changes via acoustic matched field processing. *Applied Acoustics*, 70(5):695 – 702, 2009.

[26] C. Tsogka, D. A. Mitsoudis, and S. Papadimitropoulos. Selective imaging of extended reflectors in two-dimensional waveguides. *SIAM J. Imaging Sci.*, 6(4):2714–2739, 2013.

[27] C. Tsogka, D. A. Mitsoudis, and S. Papadimitropoulos. Partial-aperture array imaging in acoustic waveguides. *Inverse Problems*, 32(12):125011, 2016.

[28] C. Tsogka, D. A. Mitsoudis, and S. Papadimitropoulos. Imaging extended reflectors in a terminating waveguide. *SIAM J. Imaging Sci.*, 11(2):1680–1716, 2018.

[29] Y. Xu, C. Mawata, and W. Lin. Generalized dual space indicator method for underwater imaging. *Inverse Problems*, 16:1761 – 1776, 2000.

[30] X. 'Peter' Zhu, P. Rizzo, A. Marzani, and J. Bruck. Ultrasonic guided waves for nondestructive evaluation/structural health monitoring of trusses. *Measurement Science and Technology*, 21(4):045701, mar 2010.